


RESEARCH ARTICLE

10.1029/2018MS001373

Special Section:

The Energy Exascale Earth System Model (E3SM)

Key Points:

- The Energy Exascale Earth System Model (E3SM) is a new climate model by the U.S. Department of Energy
- E3SM ocean and ice components use unstructured horizontal meshes for variable-resolution simulations
- The 310-year E3SM simulations agree well with observations in ocean currents and sea ice coverage

Correspondence to:

M. R. Petersen,
mpetersen@lanl.gov

Citation:

Petersen, M. R., Asay-Davis, X. S., Berres, A. S., Chen, Q., Feige, N., Hoffman, M. J., et al. (2019). An evaluation of the ocean and sea ice climate of E3SM using MPAS and interannual CORE-II forcing. *Journal of Advances in Modeling Earth Systems*, 11, 1438–1458. <https://doi.org/10.1029/2018MS001373>

Received 22 MAY 2018

Accepted 5 APR 2019

Published online 24 MAY 2019

An Evaluation of the Ocean and Sea Ice Climate of E3SM Using MPAS and Interannual CORE-II Forcing

Mark R. Petersen¹, Xylar S. Asay-Davis², Anne S. Berres³, Qingshan Chen⁴, Nils Feige³, Matthew J. Hoffman², Douglas W. Jacobsen², Philip W. Jones², Mathew E. Maltrud², Stephen F. Price², Todd D. Ringler², Gregory J. Streletz^{3,5}, Adrian K. Turner², Luke P. Van Roekel², Milena Veneziani², Jonathan D. Wolfe², Phillip J. Wolfram², and Jonathan L. Woodring³

¹Computational Physics and Methods (CCS-2), Los Alamos National Laboratory, Los Alamos, NM, USA, ²Fluid Dynamics and Solid Mechanics (T-3), Los Alamos National Laboratory, Los Alamos, NM, USA, ³Applied Computer Science (CCS-7), Los Alamos National Laboratory, Los Alamos, NM, USA, ⁴School of Mathematical and Statistical Sciences, Clemson University, Clemson, SC, USA, ⁵Department of Computer Science, University of California, Davis, CA, USA

Abstract The Energy Exascale Earth System Model (E3SM) is a new coupled Earth system model sponsored by the U.S. Department of Energy. Here we present E3SM global simulations using active ocean and sea ice that are driven by the Coordinated Ocean-ice Reference Experiments II (CORE-II) interannual atmospheric forcing data set. The E3SM ocean and sea ice components are MPAS-Ocean and MPAS-Seoice, which use the Model for Prediction Across Scales (MPAS) framework and run on unstructured horizontal meshes. For this study, grid cells vary from 30 to 60 km for the low-resolution mesh and 6 to 18 km at high resolution. The vertical grid is a structured z-star coordinate and uses 60 and 80 layers for low and high resolution, respectively. The lower-resolution simulation was run for five CORE cycles (310 years) with little drift in sea surface temperature (SST) or heat content. The meridional heat transport (MHT) is within observational range, while the meridional overturning circulation at 26.5°N is low compared to observations. The largest temperature biases occur in the Labrador Sea and western boundary currents (WBCs), and the mixed layer is deeper than observations at northern high latitudes in the winter months. In the Antarctic, maximum mixed layer depths (MLD) compare well with observations, but the spatial MLD pattern is shifted relative to observations. Sea ice extent, volume, and concentration agree well with observations. At high resolution, the sea surface height compares well with satellite observations in mean and variability.

1. Introduction

The purpose of this manuscript is to introduce a new global coupled climate model, the Energy Exascale Earth System Model (E3SM Project, DOE, 2018, <https://github.com/E3SM-Project/E3SM>), to the research community by describing ocean-sea ice simulations forced by a data atmosphere. E3SM is the first climate model where all components are capable of regional refinement of the horizontal grid. This new capability allows researchers to place high resolution where it is most beneficial for the topic at hand, be it regional climate studies, coastal impacts, or melting under ice shelves.

Several advancements were required for a variable-resolution climate model to come to fruition. In the ocean, a critical step was the discretization of the primitive equations on unstructured meshes that conserves mass, energy, and potential vorticity in the same way as the continuous equations (Ringler et al., 2010; Thuburn et al., 2009). This new ocean formulation is on an Arakawa “C-grid” (Arakawa & Lamb, 1977) with normal vectors on edges, rather than the “B-grid” with full vectors on vertices as used by the Parallel Ocean Program (POP; Smith et al., 2010). For the sea ice model, the variational divergence of stress operator of Hunke and Dukowicz (2002) was adapted to the Voronoi cells of Model for Prediction Across Scales (MPAS) meshes, from the quadrilateral cells used by the Los Alamos sea ice model (CICE). An unstructured mesh requires a completely new array structure, as horizontal neighbors are defined by new pointer variables rather than the next *i* or *j* index, as in structured mesh codes. The added complexity of an unstructured mesh extends to other parts of the code, including halos for message passing, higher order stencils, tensor operations, and interpolation.

©2019. The Authors.

This is an open access article under the terms of the Creative Commons Attribution-NonCommercial-NoDerivs License, which permits use and distribution in any medium, provided the original work is properly cited, the use is non-commercial and no modifications or adaptations are made.

These fundamental changes motivated the development of a completely new code base, MPAS, which is an unstructured mesh framework for climate model components. E3SM includes MPAS components for ocean, sea ice, and land ice. The E3SM Atmosphere Model uses the High Order Method Modelling Environment spectral element dynamical core (Evans et al., 2013), which also supports regionally refined grids. The transition to unstructured meshes also required the development of new tools for analysis, initial condition generation, and coupling. This undertaking, by the U.S. Department of Energy and collaborators, began with the creation of individual components from 2010 to 2014 (Petersen et al., 2015; Ringler et al., 2013), and then coupling and simulations within the new E3SM (formerly named the Accelerated Climate Model for Energy).

So was it worth it? After decades of development, global climate models on structured grids are highly refined for both physical fidelity and computational performance and set a high bar for success for a new Earth System Model (ESM). Yet, given successes at the global scale, combined with advances in computing power, there is now a transition from questions about *global mean* changes, embodied by the first five reports by the Intergovernmental Panel on Climate Change (IPCC; Stocker et al., 2013), to impact assessment at regional and decadal scales. Unstructured meshes bring significant new potential to enable regionally refined simulations in ESMs given the lower computational cost relative to global high resolution. Quantifying regional alterations in climate processes and future impacts requires both high resolution and ensembles of simulations, making the computational efficiency gained by placing the majority of grid cells in regions of interest highly desirable. The investment in E3SM has produced new methods and codes in order to enable this new capability for scientific inquiry and risk assessment. This paper is a first step in evaluating the new model.

Here we present standard “CORE-forced” simulations, which have active ocean and sea ice components, but data atmospheric forcing and run-off from the Coordinated Ocean-ice Reference Experiments II (CORE-II) forcing data set (Large & Yeager, 2009). Validation and model intercomparisons are critical steps for any new climate model, and the CORE-II standard offers a rich variety of literature to compare with other IPCC-class models as well as observations over the reanalysis period (e.g., Danabasoglu et al., 2014a, 2016; Downes et al., 2015; Griffies et al., 2014). To evaluate the multiresolution capability of the E3SM ocean component, we present results from two meshes: an eddy closure (EC) mesh that parameterizes mesoscale eddies; and a Rossby Radius of deformation scaling (RRS) mesh that resolves mesoscale eddies over most of the globe. In these meshes, grid cell areas vary across the globe by a factor of 2 or 3. The purpose of this study is to demonstrate the capability of E3SM on relatively uniform global meshes that are similar to previous studies with structured ocean model grids. Simulations with more dramatic variations in resolution, like those in Sein et al. (2017), will be explored in future work.

The manuscript is organized as follows. Section 2 describes model components, resolution, and forcing. Section 3 presents analysis from five CORE cycles of a lower-resolution simulation, plus 35 years of high-resolution results, and conclusions are presented in section 4.

2. Model Configuration

All MPAS components (<https://github.com/MPAS-Dev/MPAS-Model>) share a common software framework for operations on the unstructured horizontal mesh, which is based on Voronoi tessellations. The MPAS framework is parallelized through the use of OpenMP, Message Passing Interface (MPI), parallel-netcdf, and the Parallel Input/Output Library (PIO). Multiple hydrodynamic cores have been produced based on generalized discretizations for the Voronoi tessellations (Ringler et al., 2010; Thuburn et al., 2009) and include a shallow-water model (Ringler et al., 2011), an ocean model (Ringler et al., 2013), a hydrostatic atmosphere (Rauscher et al., 2012), a nonhydrostatic atmosphere (Skamarock et al., 2012), a sea ice model, and a land ice model (Hoffman et al., 2018).

2.1. Ocean Component

MPAS-Ocean is the ocean component of E3SM (version 1). MPAS-Ocean has been previously validated as a stand-alone ocean model with global high-resolution and variable-resolution simulations (Ringler et al., 2013) and with standard idealized test cases (Petersen et al., 2015; Reckinger et al., 2015; Ringler et al., 2017; Wolfram et al., 2015). It is a finite volume discretization of the primitive equations and invokes the hydrostatic, incompressible, and Boussinesq approximations on a staggered C-grid.

Grid cells are typically near hexagons (Figure 1), but cells may have any number of sides; the algorithms and code are identical for all cell shapes. The horizontal discretization of the continuous equations was

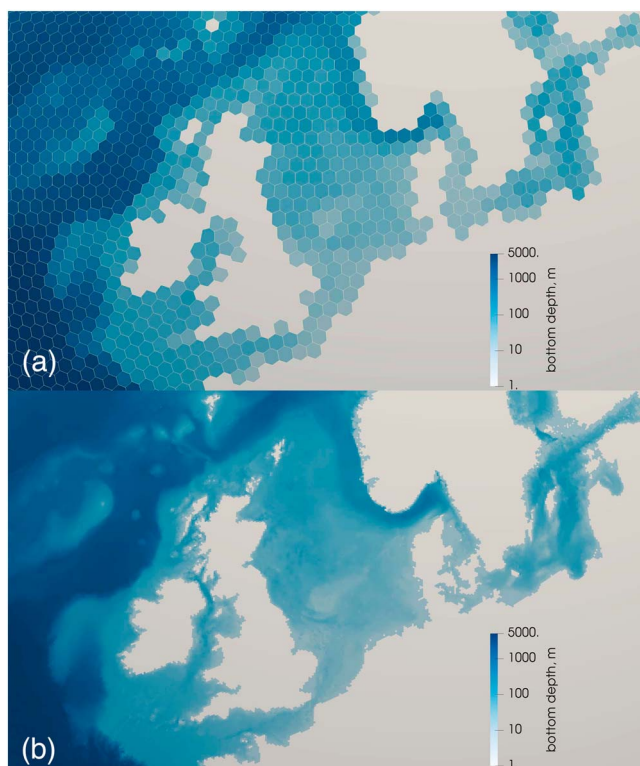


Figure 1. Examples of ocean meshes around the North Sea region for low resolution (EC60to30, a) and high resolution (RRS18to6, b) where hexagons are fine enough that they are indistinguishable from figure pixels.

derived using mimetic methods and guarantees conservation of mass, potential vorticity, and energy (Ringler et al., 2010; Thuburn et al., 2009), making it well suited to the simulation of mesoscale eddies. The tracer advection scheme is the quasi third-order flux corrected transport scheme (Skamarock & Gassmann, 2011) with separate limiting in the horizontal and vertical. The MPAS-Ocean time stepping method is split explicit, where the barotropic component is subcycled within each baroclinic time step.

The MPAS-Ocean vertical grid is structured and uses an arbitrary Lagrangian-Eulerian method with several choices of vertical coordinates (Petersen et al., 2015). The simulations presented here use z -star, where the layer thicknesses of the full column expand and contract with the sea surface height (SSH; Adcroft & Campin, 2004). The prognostic volume equation of state includes surface fluxes from the coupler; thus, virtual salinity fluxes are not needed.

Vertical mixing is computed implicitly at the end of each time step, where the CVMix library (<https://github.com/CVMix/CVMix-src>, <https://doi.org/10.5281/zenodo.1000800>) is called to compute the vertical diffusion and viscosity in each column using the K-profile parameterization (KPP; Large et al., 1994). KPP itself has been implemented in numerous ocean circulation models. Each implementation makes slightly distinct physical and numerical choices. Sometimes, these implementation choices have unintended consequences that can negatively impact the KPP boundary layer simulation. These issues motivated the development of the CVMix library, which is a suite of standardized vertical mixing parameterizations for implementation in a three-dimensional ocean circulation model. Our configuration of KPP is based on the results of an intermodel comparison against large eddy simulations (Van Roekel et al., 2018).

A mesoscale eddy parameterization is needed for the lower-resolution mesh (EC60to30), so the current simulations employ the classic Gent and McWilliams (1990) eddy transport (GM) parameterization. The GM coefficient was tuned, in part, to help match observational estimates of transport through the Drake Passage, resulting in a value of $600 \text{ m}^2/\text{s}$ for the bolus component for the standard simulation. A full set of five core cycles was also run with a higher value of $1,800 \text{ m}^2/\text{s}$ but resulted in very weak Southern Ocean transports and Atlantic overturning. Previous publications have explored alternative implementations of GM with spatially variable coefficients in idealized (Chen et al., 2016; Ringler & Gent, 2011) and realistic

domains (Gent & Danabasoglu, 2011), but a constant value was used here for simplicity and comparison with other CORE-forced studies (Danabasoglu et al., 2014a; Griffies et al., 2009). The Redi component (Redi, 1982), which adds diffusion along isopycnal layers was set to zero for this set of simulations. In contrast to the EC60to30, the high-resolution RRS18to 6 simulation directly resolves much of the mesoscale eddy activity and consequently the GM parameterization is not needed.

Initial conditions for temperature and salinity are interpolated from the Polar Science Center Hydrographic Climatology, version 3 (Steele et al., 2001). MPAS-Ocean has an “init mode” capability in the same executable as the forward model, which includes scalable file writing and interpolation tools to produce initial conditions. This is required at high resolution, where the file size of the ocean initial condition is 29 GB. The ocean is started from rest and spun up for several months, forced by an annual average wind stress and restoring of temperature and salinity at the top layer, in order to create an initial condition for E3SM.

Additional features that are available in MPAS-Ocean but not used in this study include Lagrangian particles (Wolfram & Ringler, 2017a, 2017b; Wolfram et al., 2015), the ability to run with sub-ice shelf ocean cavities in Antarctica (Asay-Davis et al., 2017), and the computation of the Eliassen-Palm flux tensor to diagnose momentum transfer due to eddy-mean flow interactions (Ringler et al., 2017; Saenz et al., 2015). MPAS-Ocean includes a full biogeochemistry module based on the Biogeochemical Elemental Cycling model developed for Community ESM (Moore et al., 2004, 2013). In situ model diagnostics are used throughout to demonstrate preparedness for next generation exascale high-performance computing (Woodring et al., 2016).

2.2. Sea Ice Component

The sea ice component of E3SM is MPAS-Seoice. MPAS-Seoice solves the same sea ice momentum equation and uses the same “B” grid (Arakawa & Lamb, 1977) and Elastic-Viscous-Plastic rheology (Hunke & Dukowicz, 1997) as the CICE sea ice model (Hunke et al., 2015), but with its divergence of internal stress operator adapted to work with the polygonal cells used by the MPAS framework, instead of the quadrilateral cells used by CICE. The divergence of stress operator uses an adaptation of the variational scheme from Hunke and Dukowicz (2002). Instead of the bilinear basis functions used in Hunke and Dukowicz (2002), MPAS-Seoice uses Wachpress basis functions (Dasgupta, 2003). MPAS-Seoice uses an incremental remapping scheme, similar to that of Dukowicz and Baumgardner (2000), Lipscomb and Hunke (2004), and Lipscomb and Ringler (2005), to transport sea ice concentration and tracers. The scheme of Lipscomb and Hunke (2004) was implemented for quadrilateral structured meshes and is used in CICE (Hunke et al., 2015). The Lipscomb and Ringler (2005) scheme was implemented for a structured Spherical Centroidal Voronoi Tessellation mesh.

MPAS-Seoice uses the same column physics and biogeochemistry code as CICE. For simulations presented here, MPAS-Seoice used the “mushy layer” vertical thermodynamics of Turner et al. (2013) and Turner and Hunke (2015), the delta-Eddington shortwave radiation scheme of Briegleb and Light (2007) and Holland et al. (2012), a level-ice melt-pond scheme (Hunke et al., 2013), the scheme for transport in thickness space of Lipscomb (2001), and representations of mechanical redistribution (Lipscomb et al., 2007).

MPAS-Seoice is coupled to MPAS-Ocean in the same way as CICE is coupled to POP in the Community ESM (Craig et al., 2012), except for several changes needed to accommodate differences in formulation between MPAS-Ocean and POP. First, MPAS-Ocean provides a mass of frazil ice formed, instead of the freezing potential to represent frazil ice formation provided by POP. MPAS-Seoice then converts the mass of frazil ice formed to a freezing potential. Second, since MPAS-Ocean’s free surface may be depressed to arbitrary depths, MPAS-Seoice provides the weight of sea ice and snow to MPAS-Ocean. This allows MPAS-Ocean to compute the appropriate depression of the ocean surface due to this weight. The ocean model returns the sea surface gradient to the sea ice model, which then calculates from it a surface tilt force. This sea surface gradient is relaxed to zero with a 1 day timescale to prevent a numerical coupling instability.

The CORE-forced simulations were started with sea ice present above 70°N and below 60°S, with an initial ice concentration of one, a thickness of 1 m, and no snow. Ice salinity was set to the profile of Bitz and Lipscomb (1999), and the ice temperature profile was set as linear between the minimum of the ice melting temperature and the air temperature at the top surface and the ocean freezing temperature at the basal surface.

Table 1
Resolutions of MPAS-Ocean and MPAS-Sea Ice

Resolution	Cell size max (km)	Cell size min (km)	Horizontal cells ($\times 10^6$)	Vertical layers	Compute (Mcpu-hrs /century)
low: EC60to30	60	30	0.23	60	0.36
high: RRS18to6	18	6	3.7	80	11.17

Note. The abbreviations correspond to the global mesh density function: EC is low resolution and requires a mesoscale eddy closure parameterization; grid cell size (km) in RRS domain scales with the Rossby Radius of deformation in latitude. Compute time was measured on a cluster of Intel Xeon Broadwell nodes (see section 2.5). EC = eddy closure; RRS = Rossby Radius of deformation scaling.

2.3. Atmospheric Forcing

The CORE-II forcing data set (Griffies et al., 2009; Large & Yeager, 2009) is the international standard for ocean-sea ice simulations within the World Climate Research Programme Coupled Model Intercomparison Project (CMIP) and is based on the National Centers for Environmental Predictions/National Center for Atmospheric Research atmospheric reanalysis with further corrections guided by observations. The CORE-II data set is commonly used by different modeling centers to evaluate ocean model performance across physically realistic forcing scenarios (e.g., Danabasoglu et al., 2014a, 2016; Downes et al., 2015; Griffies et al., 2014). The CORE-II climate simulations are a benchmark that is well suited to provide short-term, seasonal and yearly climatologies, allowing assessment of oceanic model dynamics within the context of other CMIP ocean models. In CMIP6 there will be an Ocean Model Intercomparison Project (Griffies et al., 2016) as part of the CMIP6-MIPS, which will use the CORE-II forcing. For this study, we use the 62-year period from 1948 to 2009.

In data-forced ocean-sea ice simulations (e.g., Danabasoglu et al., 2014a), it is necessary to linearly restore sea surface salinity (SSS) toward climatology in order to maintain a robust Atlantic Meridional Overturning Circulation (AMOC). For the high- and low-resolution simulations we have chosen a piston velocity of 50 m/year (equivalent to a time scale of 1 year if we assume a depth scale of 50 m) as our constant of proportionality, which is consistent with the majority of ocean models described in Danabasoglu et al. (2014a). This restoring term is applied as a salinity source in the top layer of the model, including under sea ice in proportion to the fraction of open water. The restoring source term is calculated at the beginning of every model day, and the global mean is removed so that it has no net effect on the total amount of salt.

2.4. Resolutions

Two model resolutions are used in this study: a low-resolution that requires a mesoscale EC parameterization (EC60to30) and a high-resolution that is mesoscale eddy resolving (RRS18to6). The specifications of the EC60to30 and RRS18to6 meshes are shown in Table 1. The EC60to30 mesh contains 235 thousand horizontal ocean cells, which is greater than a standard $1/2^\circ$ uniform grid. Grid cell size varies from 30 to 60 km, with enhanced resolution in equatorial and polar regions in order to resolve important equatorial dynamics such as Tropical Instability Waves (Figure 2). This mesh includes 60 vertical layers ranging from 10 m thick at the surface to 250 m thick in the deep ocean.

The high-resolution mesh cell spacing follows the “Rossby Radius Scaling.” The RRS18to6 mesh was designed to be similar to a $1/10^\circ$ grid, with grid cell size varying with latitude in proportion to the Rossby radius of deformation. Thus, away from continental shelves, the mesh resolution is roughly equivalent to the size of mesoscale eddies, facilitating the model to resolve mesoscale eddy activity within the Antarctic Circumpolar Current (ACC). The resolution for this RRS18to6 mesh ranges from 18 km near the equator to 6 km at the poles and includes 80 vertical layers ranging from 2 m at the surface to 220 m at depth.

The horizontal meshes were created with an iterative, parallel algorithm for the construction of Spherical Centroidal Voronoi Tessellations (Jacobsen et al., 2013). Global meshes are not coastal conforming, that is, cell edges do not exactly line up along the coastline. Rather, a mesh is generated from a grid cell density function on the full sphere. Then, grid cells with cell centers on the landward side of coastlines (Land regions are taken from a combination of Natural Earth [<http://www.naturalearthdata.com/>] north of 60°S and Bedmap2

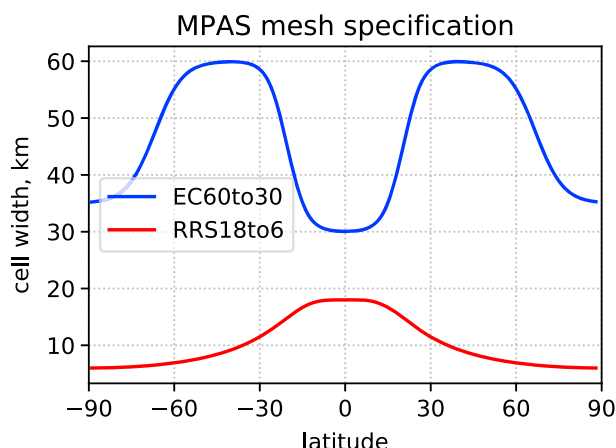


Figure 2. Grid cell size of the unstructured mesh as a function of latitude for the two standard resolutions. MPAS = Model for Prediction Across Scales.

[Fretwell et al., 2013] south of 60°S.) are culled. Sea ice and ocean components are run on identical meshes so that no horizontal interpolation is required to compute fluxes between these components. In the ocean, the bottom depth of each grid cell is generated from a combination ofETOPO1 (Amante & Eakins, 2009) north of 60°S blended with Bedmap2 (Fretwell et al., 2013) south of 60°S. Each column uses a partial bottom cell and a minimum thickness of three cells in shallow regions. Single-cell-wide channels are removed from the mesh in polar regions, as the sea ice model is discretized on an Arakawa B-grid (Arakawa & Lamb, 1977) and requires two grid cells for sea ice advection. In the low-resolution mesh, the depths of grid cells at the sills of the Strait of Gibraltar, English Channel, and outlets of the Red Sea, Baltic Sea, and Persian Gulf are set to the maximum sill depth for that passage to provide adequate cross-sectional area for transport.

2.5. Performance

E3SM is designed for high-performance computing architectures. Each component may be scaled up to tens of thousands of processing cores using a combination of message passing (MPI) and threading (OpenMP). E3SM compiles into a single executable, but each model component may

be run either in its own separate partition of MPI ranks, or stacked within the same partition. The processor layout is adjusted and load-balanced in order to maximize overall throughput of the coupled system, measured in simulated years per wall-clock day (SYPD). The simulations presented here were performed on a project-owned partition of the Blues cluster at Argonne National Laboratory's Laboratory Computing Resource Center. Each node in this partition consists of two 18-core Intel Xeon "Broadwell" (E5-2697V4, 2.3 GHz) processors and 64-GB dynamic random-access memory, connected through an Fourteen Data Rate InfiniBand network. The low-resolution configuration used 1,200 cores for the ocean in one partition, and 320 cores in a second partition that shared sea ice, coupler and data components. Similarly, the high-resolution simulation was partitioned between 3,600, 3,200, and 3,600 cores for ocean, sea ice, and coupler. The throughput is 10.9 and 0.72 SYPD for low and high resolution, which translates to 0.34 and 11.17 million CPU hours per century. The coupling interval is 0.5 hr for each resolution. While the performance is respectable, substantial ongoing work is directed at improving performance of the MPAS components, including message-passing optimization, thread optimization, vectorization, and Graphics Processing Unit acceleration.

2.6. Analysis

Because computational performance is likely to continue to increase faster than I/O and file system performance, we have chosen to perform much of our analysis in situ via an analysis member approach. In traditional analysis, data are written to disk and then in a postprocessing step is read back into memory for analysis computations. MPAS-Ocean's in situ analysis members, in contrast, do not require a postprocessing step but are instead computed while MPAS-Ocean is running to produce computationally and data intensive model diagnostics. The analysis member approach has already allowed computation of challenging diagnostics that would be computationally intractable if dependent upon postprocessing analysis of data output, for example, the Okubo-Weiss eddy diagnostics (Woodring et al., 2016), the Eliassen-Palm flux tensor (Ringler et al., 2017; Saenz et al., 2015), and Lagrangian particle tracking used for the computation of diffusivity (Wolfram & Ringler, 2017a, 2017b; Wolfram et al., 2015). This online analysis member approach is also being used within E3SM to compute priority diagnostics to assess simulation quality for fields such as the AMOC and MHT.

We have also built a Python-based tool, MPAS-Analysis (<https://github.com/MPAS-Dev/MPAS-Analysis>), for performing postprocessed analysis and plotting. With the help of NetCDF Operators (<https://github.com/nco/nco>), MPAS-Analysis can compute climatologies, extract time series, and perform interpolation to common reference grids (via remapping operations). The tool supports comparisons between simulation results and a wide variety of observational data sets on either latitude/longitude or polar stereographic grids (the latter being common for many data sets covering polar regions). Alternatively, simulations can be compared against one another to explore the effects of changing parameters, resolution, model physics, meshes, and

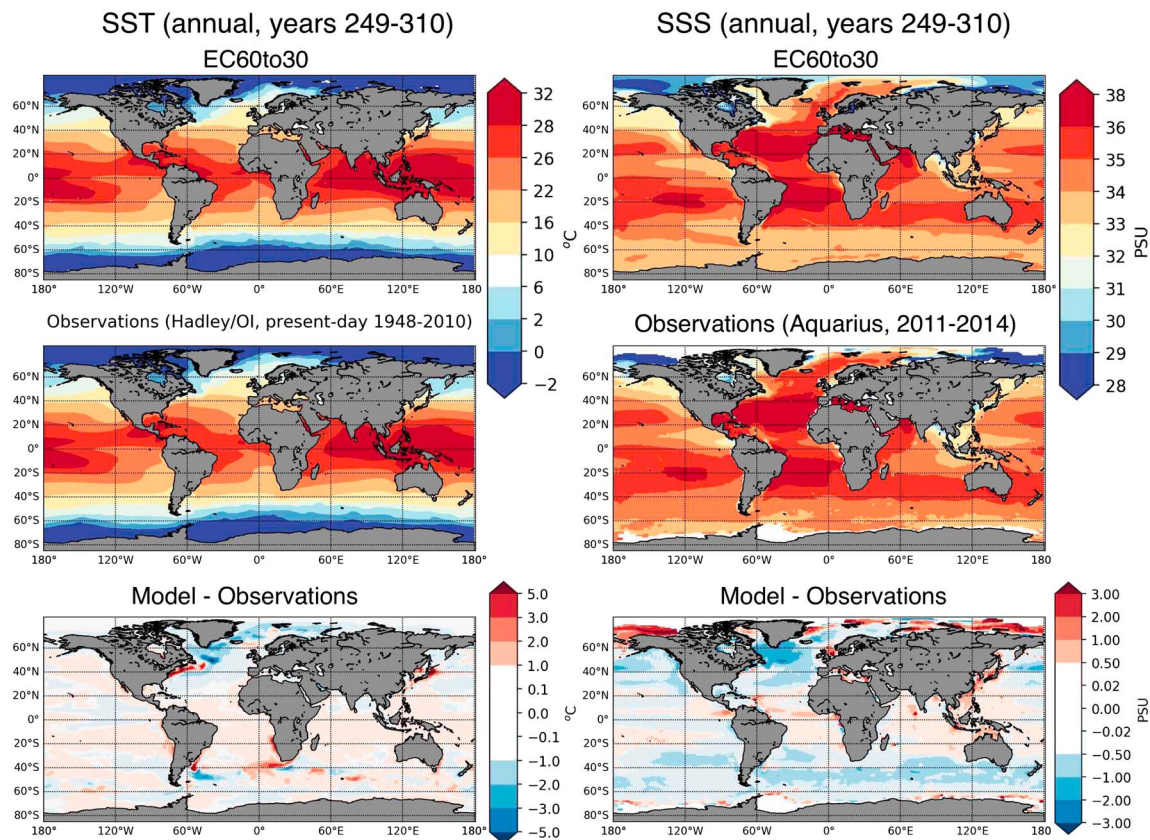


Figure 3. Sea surface temperature ($^{\circ}\text{C}$, left column) and sea surface salinity (psu, right column) compared to observations. SSS = sea surface salinity; SST = sea surface temperature.

much more. MPAS-Analysis breaks each analysis task into a large number of modular subtasks, allowing each task or subtask to run in parallel, making the production of hundreds of plots relatively efficient. Since MPAS-Analysis can parse the E3SM namelist options and input/output streams of any MPAS model component, tasks are automatically included or excluded, depending on which analysis members and model physics were included in the simulation. The final product of an MPAS-Analysis run is both a user-friendly website with image galleries of all plots and a set of NetCDF files that contain the postprocessed data used to create each plot.

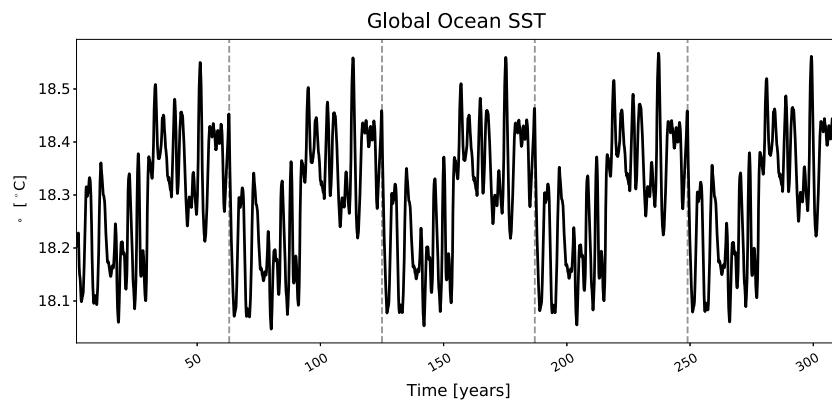


Figure 4. Sea surface temperature (SST, $^{\circ}\text{C}$), globally averaged. Vertical lines correspond to Coordinated Ocean-ice Reference Experiments II cycle boundaries.

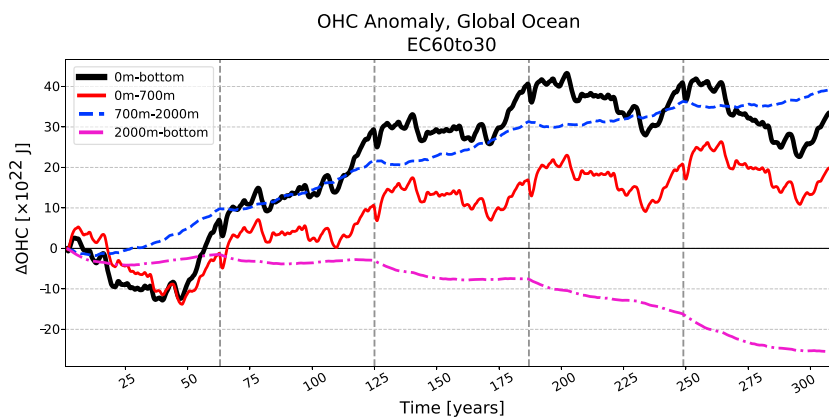


Figure 5. Ocean heat content (OHC) anomaly (10^{22} J), globally averaged, partitioned by depth. Negative trends indicate heat loss from the ocean. Vertical lines correspond to Coordinated Ocean-ice Reference Experiments II cycle boundaries.

3. Results

3.1. Temperature, Salinity, and Heat Content

A first assessment of the simulated global ocean surface conditions is made by considering the annual average (computed over the last CORE cycle) SST and SSS (upper panels in Figure 3), compared with SST observations from the merged Hadley Center-National Oceanic and Atmospheric Administration Optimum Interpolation data set (Hurrell et al., 2008) for the period 1948–2010 and SSS observations from the National Aeronautics and Space Administration Aquarius Satellite for the period 2010–2014 (see middle panels of Figure 3 for the observational fields, while the lower panels show the model-observation biases). Overall, the model exhibits a warm SST bias between the midlatitudes and the equator, with mean values smaller than 1 °C in most places except for the regions north of the Gulf Stream and Kuroshio Currents, where biases are 5 °C or larger. Negative SST biases are found in the Nordic Seas and Labrador Sea, which could be associated with a shift in the position of the modeled Gulf Stream and Kuroshio currents or associated with overly extended sea ice coverage. The cold bias in the Labrador Sea is also associated with a fresh bias in SSS (lower right panel in Figure 3). The globally averaged SST, shown in Figure 4, shows a very stable surface temperature with the expected interannual variability (e.g., the sudden changes in each mid-CORE cycle are due to the mid-1970s North Pacific regime shift; Hare & Mantua, 2000).

The trends of ocean heat content (OHC) integrated over a number of depth ranges are shown in Figure 5, while OHC and salinity anomalies with depth are presented in Figure 6. Anomalies are computed with respect to the first year of the simulation in Figure 5 and with respect to the 4th CORE cycle last year (year 248) in Figure 6. The total (surface to bottom) OHC and upper ocean OHC (0–700 m) are stable after the first three CORE cycles. The OHC integrated over 700–2,000 m shows a positive trend that is counteracted by heat loss in the bottom layers. The salinity anomaly trend during the last CORE cycle shows the accumulation

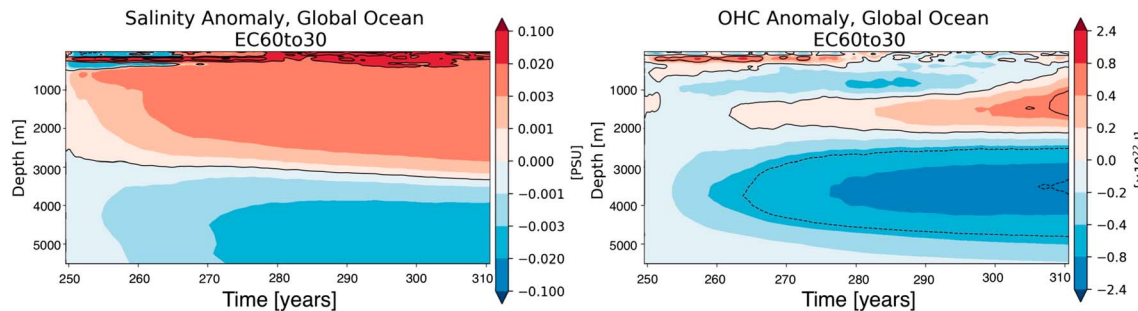


Figure 6. Global average anomaly compared with year 248 of ocean heat content (OHC, 10^{22} J, right) and salinity (psu, left) as functions of depth, for the fifth Coordinated Ocean-ice Reference Experiments cycle.

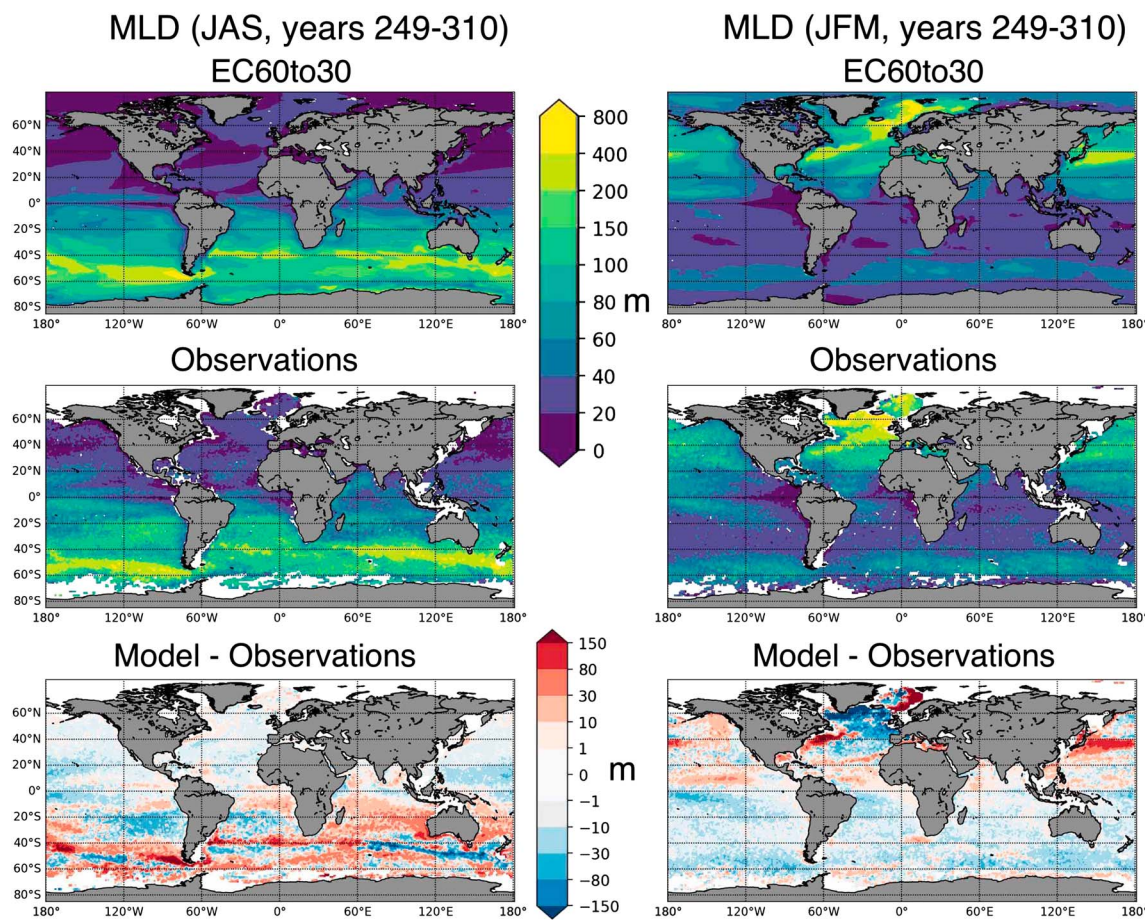


Figure 7. Mixed layer depth (MLD, m) compared to observations from ARGO climatology (Holte et al., 2017).

of a salty anomaly in all of the upper 2,000 m, but especially at the surface and between 300- and 1,000-m depth.

3.2. MLD

Figure 7 shows the mean MLD, which is based on the 0.03 kg/m^3 density threshold criterion (de Boyer Montégut et al., 2004) compared to an ARGO climatology (Holte et al., 2017) for Boreal and Austral winter (Figures 7a and 7b, respectively). There is a significant shallow bias covering much of the North Atlantic, which is consistent with the modeled surface fresh bias (Figure 3). The largest of these shallow biases are

in the Labrador and Irminger Seas, which are key locations of North Atlantic Deep Water formation. The shallow bias in the Labrador Sea is broadly consistent with a number of other CORE forced models (see Danabasoglu et al., 2014b, their Figure 13). The CORE forced models with shallower Boreal winter MLD experience weaker AMOC strengths. This is also seen in MPAS-Ocean (see Figure 10). In contrast, the MLD is too deep in the northern WBCs and their extension regions, as well as in the Norwegian Sea. Overall, there is a shallow bias throughout the Southern Hemisphere in Austral summer.

In Austral winter, the model exhibits a significant deep MLD bias across most of the Southern Hemisphere. However, the E3SM longitudinal distribution of maximum MLD between 45°S and 65°S in the Southern Ocean is very consistent with the ARGO climatology (Figure 8), suggesting the bias is an offset in the latitudinal position of the deepest MLD in the model compared to the data. However, at high resolution, the longi-

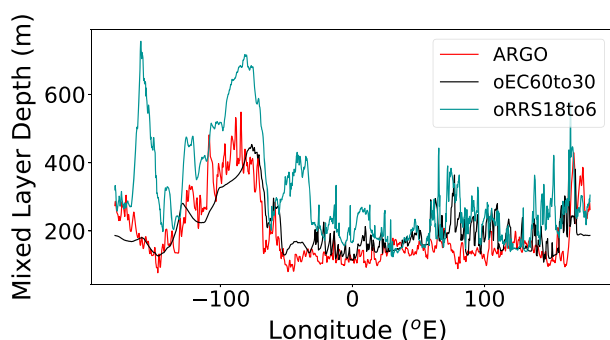


Figure 8. Maximum mixed layer depths (m) between 65°S and 45°S as a function of longitude for both resolutions, compared to ARGO observations.

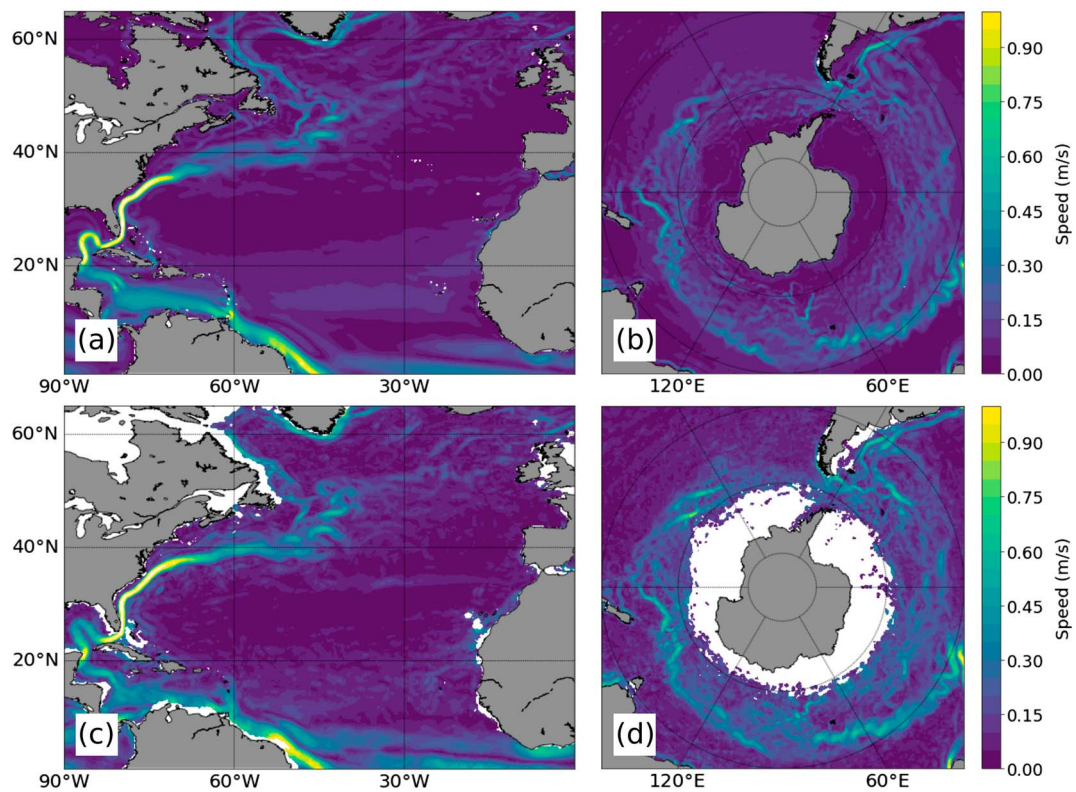


Figure 9. Mean surface currents (m/s) in Atlantic Ocean (a and c) and Southern Ocean (b and d). The top row is from the high-resolution simulation, and the bottom is from the surface drifter climatology of Laurindo et al. (2017).

tudinal distribution of modeled (Figure 8) MLD are deeper than observed. In the Northern Hemisphere, the summer bias is typically slightly shallow and quite small in magnitude.

3.3. Ocean Currents and Transport

Figure 9 shows the surface currents for two regions at high resolution (top panels) and a surface drifter climatology (Laurindo et al., 2017; bottom panels). When mesoscale eddies are resolved the strength of the Gulf Stream and separation compare well with observations, consistent with previous studies (e.g., Maltrud & McClean, 2005). The Southern Ocean surface currents in the RRS18to6 configuration are close to observations.

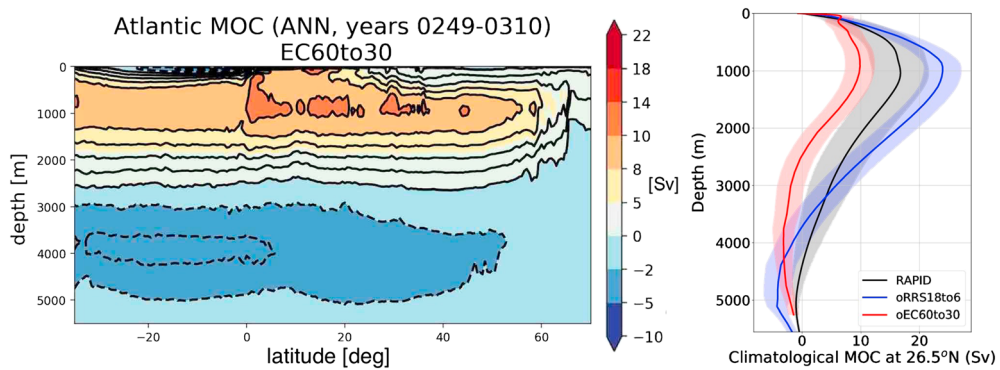


Figure 10. Meridional overturning stream function (Sv) versus latitude and depth for the EC60to30 with a GM coefficient of $600 \text{ m}^2/\text{s}$ (left) and as a function of depth at 26.5°N for both resolutions (right). These are time averages of the fifth core cycle for EC60to30, of years 25–35 for the RRS18to6, and of 2004 to 2016 for the RAPID array. MOC = Meridional Overturning Circulation.

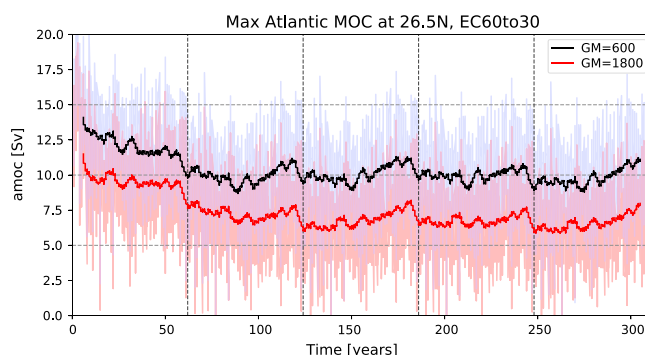


Figure 11. Maximum meridional overturning (Sv) at 26.5°N versus time for two values of the GM parameter (κ) in units of square meters per second. Light shading shows the monthly average, and dark lines are a 5-year running average. Vertical lines are the boundaries of the 62-year Coordinated Ocean-ice Reference Experiments cycles. MOC = Meridional Overturning Circulation.

The strong agreement between drifter observations and model output at high resolution indicates the capability of MPAS-Ocean to adequately resolve WBCs and geostrophic jets such as the ACC. The emergence of this capability at high resolution is consistent with these current systems being dependent on mesoscale eddy activity (e.g., Kirtman et al., 2012; Maltrud & McClean, 2005). Thus, it is not surprising that the low resolution E3SM configuration is unable to accurately simulate the WBCs and the ACC (not shown).

Figure 10 shows the AMOC averaged over the final CORE cycle for the low resolution case, and years 25–35 of the high-resolution run. The low-resolution AMOC (which is the sum of the Eulerian mean and bolus components) is quite weak, with a maximum transport of about 10 Sv. When compared with the simulations described in Danabasoglu et al. (2014a), this run is at the low end of overturning strength.

Although the AMOC is weak in the low-resolution run, it is stable over the final three CORE cycles, as can be seen in the time series of maximum strength at the RAPID location (26.5°N; Figure 11). The weak overturning is consistent with the generally sluggish North Atlantic current transports

in the low-resolution case (Table 2) but is likely due to a combination of interrelated effects, such as the GM coefficient, SSS restoring strength, vertical mixing, and model bathymetry. For example, decreasing the GM coefficient from 1,800 to 600 m²/s increased the AMOC at 26.5°N by 3 Sv (Figure 11). In another sensitivity

Table 2

Transport of Major Current Systems: Simulated Time-Mean Transports in Sverdrups Through Common Sections Are Compared to Observational Estimates

Transect location	EC60to30 GM = 1,800	EC60to30 GM = 600	RRS18to6	Observations	Observation reference
Drake Passage	89.8 ± 16.8	127.3 ± 10.6	128.2 ± 8.7	173.0 ± 10.0	Donohue et al. (2016)
				130.0 ± 20.0	Nowlin & Klinck, 1986 (1986) and Whitworth & Peterson, 1985 (1985)
Tasmania-Ant	103.3 ± 19.1	139.4 ± 12.7	147.2 ± 8.3	157.0 ± 10.0	Ganachaud (2003) and Ganachaud and Wunsch (2000)
Africa-Ant	88.4 ± 16.8	126.0 ± 10.6	129.6 ± 8.5	150.0 ± 30.0	Ganachaud (2003) and Ganachaud and Wunsch (2000) ^a
Antilles Inflow	-14.8 ± 2.9	-16.1 ± 3.0	-26.9 ± 4.7	-18.4 ± 4.7	Johns et al. (2002) and Roemmich (1981)
Mona Passage	-1.7 ± 1.0	-1.4 ± 1.3	-1.0 ± 1.2	-2.6 ± 1.2	Johns et al. (2002) and Roemmich (1981)
Windward Passage	1.0 ± 2.0	-0.2 ± 2.3	3.3 ± 4.8	6.0 ± 3.0	Johns et al. (2002) and Roemmich (1981)
Florida-Cuba	15.4 ± 1.4	15.4 ± 1.4	24.5 ± 3.5	31.0 ± 1.5	Johns et al. (2002) and Roemmich (1981)
Florida-Bahamas	15.1 ± 1.1	17.6 ± 1.6	30.1 ± 2.7	31.5 ± 1.5	Johns et al. (2002) and Roemmich (1981)
Indonesian Throughflow	-11.0 ± 3.6	-10.2 ± 3.7	-13.4 ± 2.8	-15.0 ± 4.0	Sprintall et al. (2009)
Agulhas	-68.7 ± 5.6	-72.2 ± 5.4	-57.7 ± 22.4	-70.0 ± 20.0	Bryden and Beal (2001)
Mozambique Channel	-18.7 ± 6.7	-15.8 ± 6.4	-22.0 ± 6.0	-16.0 ± 13.0	van der Werf et al. (2010)
Bering Strait	0.9 ± 0.5	1.1 ± 0.5	1.5 ± 0.5	0.8 ± 0.3	Roach et al. (1995)
Lancaster Sound	0.2 ± 0.3	0.3 ± 0.4	1.6 ± 0.4	0.8 ± 0.3	Prinsenberg and Hamilton (2005)
Fram Strait	-2.5 ± 1.1	-3.5 ± 1.2	-1.3 ± 1.3	-3.0 ± 3.0	Schauer et al. (2004)
Robeson Channel	0.0 ± 0.0	0.0 ± 0.0	-1.1 ± 0.4	-0.7 ± 0.2	Maltrud and McClean (2005)

Note. Simulated transports are of the form mean \pm standard deviation, while observed transports are of the form best estimate \pm observational error. Positive values are north and eastward. These are time averages of the fifth core cycle for EC60to30 and of years 25–35 for the RRS18to6. The EC60to30 run with a GM bolus coefficient of 600 m²/s was the primary simulation, and the high GM value of 1,800, which has much lower Southern Ocean transports, is shown for comparison.

^aEstimates from publication.

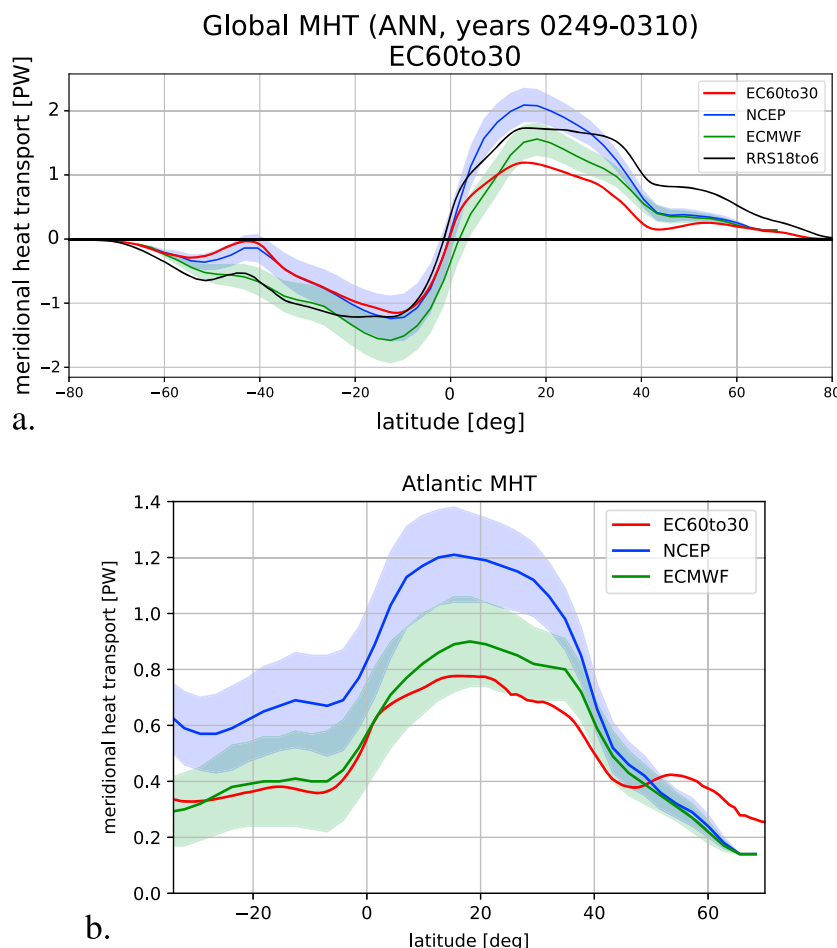


Figure 12. Meridional heat transport (PW) as a function of latitude for two resolutions, compared to mean reanalysis climatology from NCEP and ECMWF (Trenberth & Caron, 2001), for the globe (a) and the Atlantic (b). Shading indicates one standard deviation from the mean. NCEP = National Centers for Environmental Predictions; ECMWF = European Centre for Medium-Range Weather Forecasts; MHT = meridional heat transport.

test, the piston velocity of SSS restoring was increased by an order of magnitude (a time scale of about 1 month), resulting in a strengthening of the AMOC by 2–3 Sv, but it negatively affected other aspects of the simulation. A spatially variable GM coefficient may improve circulation in future simulations (Gent & Danabasoglu, 2011). Figure 11 may be directly compared to other ocean models in Figure 1 of Danabasoglu et al. (2014a). E3SM ranges with a GM value of 600 ranges from 9 to 11 Sv over the last three CORE cycles.

Another factor that likely contributes to the weak AMOC is the lack of deep convection in the Labrador and Irminger Seas (evidenced by a shallow MLD bias in section 3.2). This leaves only the Iceland and Norwegian Seas as sources of North Atlantic Deep Water formation. The water mass characteristics of the Deep WBC at 26°N are consistent with the relatively warm water formed in the Iceland Basin mixed with cold overflow from Denmark Strait and the Faroe-Iceland Ridge. However, without extra model diagnostics it is not clear what fraction of the Deep WBC transport is due to annual formation rates, and how much is recirculation.

In contrast to the sluggishness of the low-resolution runs, the high-resolution case has a maximum transport (23 Sv) on the high side of the observed value at RAPID and has a somewhat deeper and enhanced southward return flow, which may be related to the short duration of the simulation. Since several of the factors that affect low resolution are not relevant in this case (GM parameterization is turned off, and the Florida Straits bathymetry is sufficiently resolved), the primary drivers of the AMOC are the SSS restoring and vertical mixing. Unlike at low resolution, there is wintertime deep convection in the Labrador and Irminger Seas.

Table 2 shows the simulated transports through a number of major channels, compared to observations. Southern Ocean transports at low and high resolution are reasonable but on the lower side of observations.

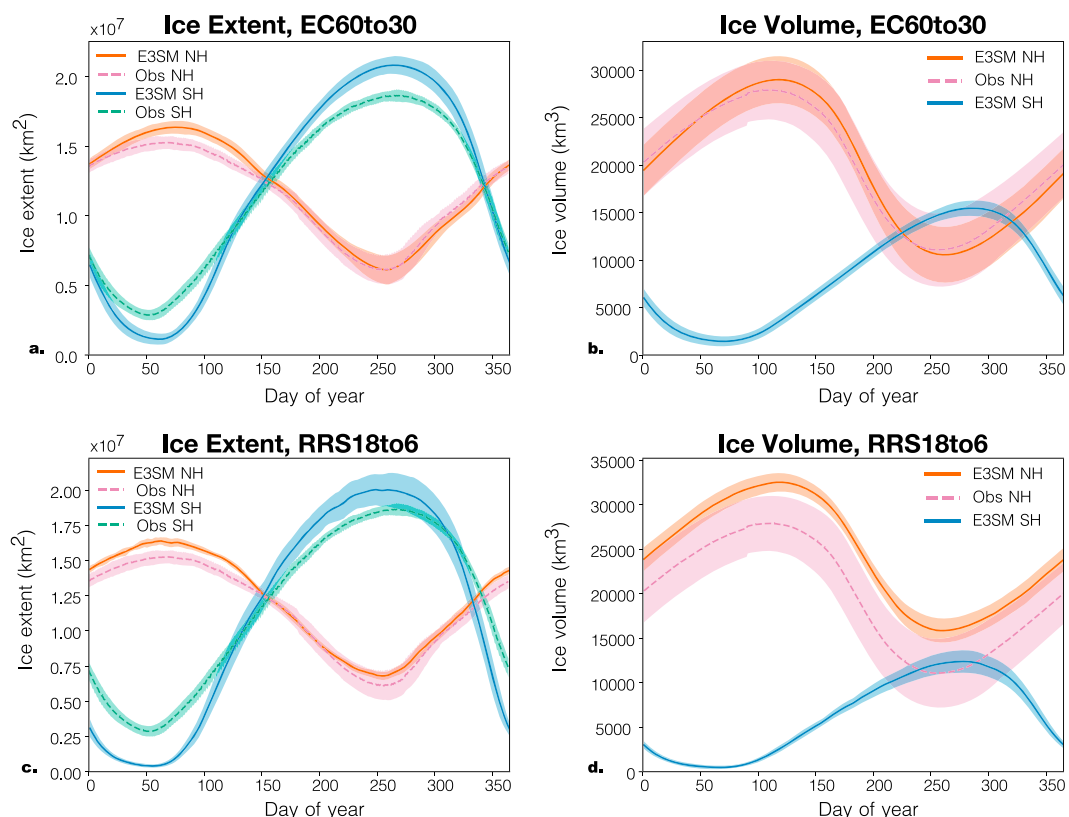


Figure 13. Total ice extent climatology (area with ice concentration $>15\%$, km^2 ; a, c) and total ice volume climatology (b, d) for the Northern and Southern Hemispheres, for E3SM results and observations, each for low resolution (a, b) and high resolution (c, d). Ice extent uses Special Sensor Microwave/Imager observations (Cavalieri & Parkinson, 2012; Parkinson & Cavalieri, 2012) and Northern Hemisphere volume observations come from Pan-Arctic Ice Ocean Modeling and Assimilation System (Schweiger et al., 2011b). The color bands represent ± 1 standard deviation of the climatology. No Southern Hemisphere observational results are shown for ice volume. E3SM = Energy Exascale Earth System Model.

Like the AMOC, Drake Passage transport is sensitive to the GM bolus parameter, where the higher value of $1,800 \text{ m}^2/\text{s}$ resulted in unreasonably weak transports. Steeper isopycnals in the meridional direction of the Southern Ocean were observed in the low-GM case, leading to increased zonal flow via the thermal wind relation.

As noted in section 2.1, alteration of the model bathymetry was performed in only five passages, all of which are associated with marginal seas. As a result of this approach, the flow through the Straits of Florida between Florida and the Bahamas is quite restricted by the representation of the islands in the low-resolution case, resulting in only 17.6 Sv of transport through this passage. Some minor changes to the bathymetry (such as requiring at least two grid cells spanning the passage) would likely increase the transport here, thus increasing the strength of the AMOC.

The global MHT (Figure 12a) reflects the overturning strength of the simulations. At coarse resolution the values are low compared to estimates, especially in the Southern Hemisphere. At high resolution, heat transport is increased in both hemispheres and is closer to estimates. At low resolution the Atlantic MHT (Figure 12b) is weak relative to other CORE forced simulation (see Danabasoglu et al., 2014b, their Figure 6), this is likely related to the weak AMOC and is consistent with the linear relationship shown in Figure 7 of Danabasoglu et al. (2014b).

3.4. Sea Ice

Sea ice has a significant effect on the ocean state. Rejection of salt during sea ice formation helps drive the thermohaline circulation (Killworth, 1983), while northward transport of fresh sea ice in the Southern Ocean affects water mass transformation Abernathey et al. (2016). Consequently, it is important to accurately

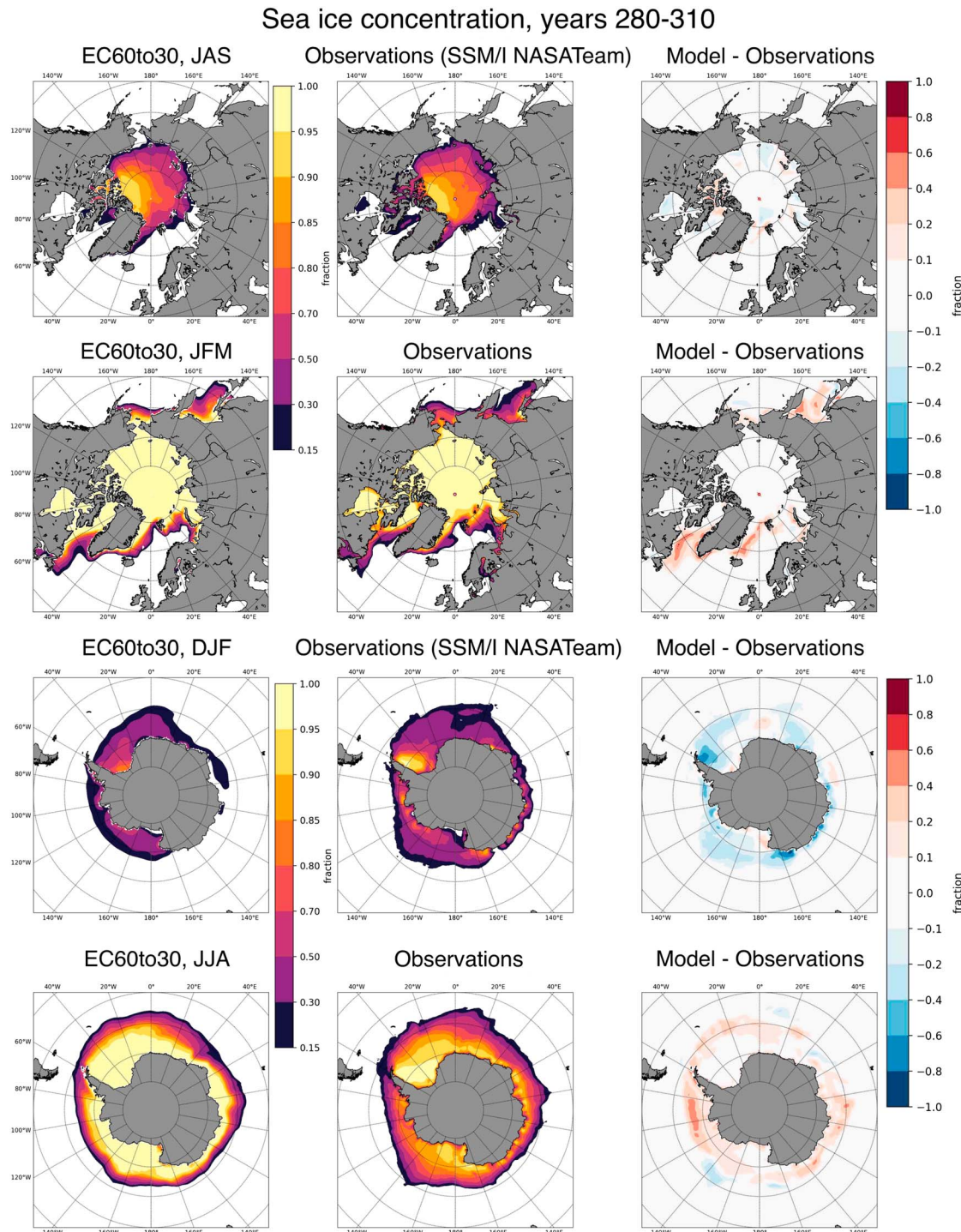


Figure 14. Sea ice concentration (normalized fraction) versus observations (SSM/I NASA Team algorithm; Cavalieri et al., 1996, updated yearly, 1996, updated yearly), where both are compared over the period 1979–2009, for the low-resolution simulation (EC60to30). SSM/I = Special Sensor Microwave/Imager; NASA = National Aeronautics and Space Administration; JAS = July–September; JFM = January–March; DJF = December–February; JJA = June–August.

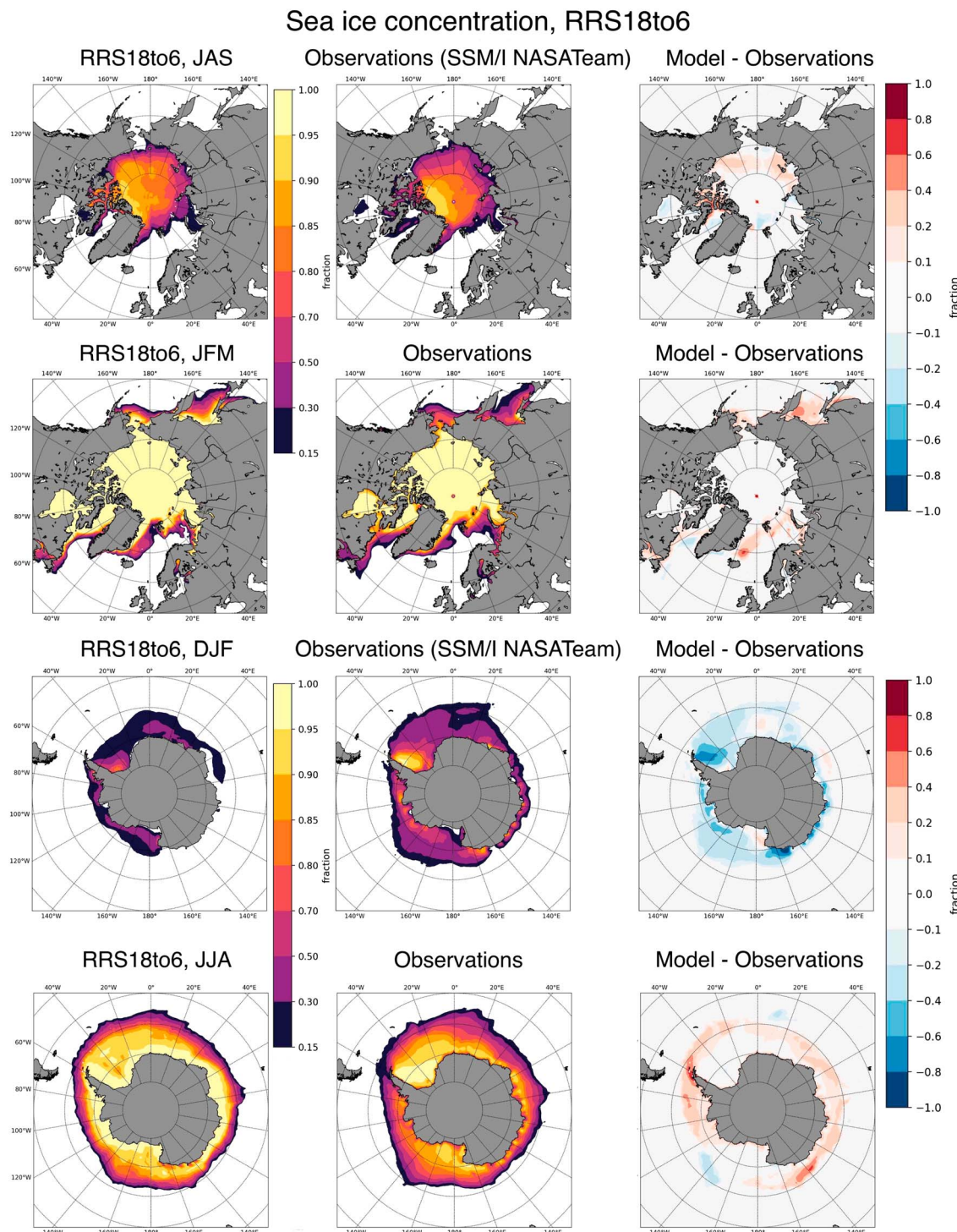


Figure 15. Same as Figure 14 but for high resolution (RRS18to6), averaged over the duration of the simulation. SSM/I = Special Sensor Microwave/Imager; NASA = National Aeronautics and Space Administration; JAS = July–September; JFM = January–March; DJF = December–February; JJA = June–August.

reproduce the sea ice state for ocean simulations. Here we examine the sea ice results for E3SM on the EC60to30 mesh.

Total sea ice extent (area with sea ice concentration greater than 15%) is shown in Figure 13 for E3SM output and compared against Special Sensor Microwave/Imager observations for the Northern (Cavalieri & Parkinson, 2012; Parkinson et al., 1999) and Southern Hemispheres (Parkinson & Cavalieri, 2012; Zwally

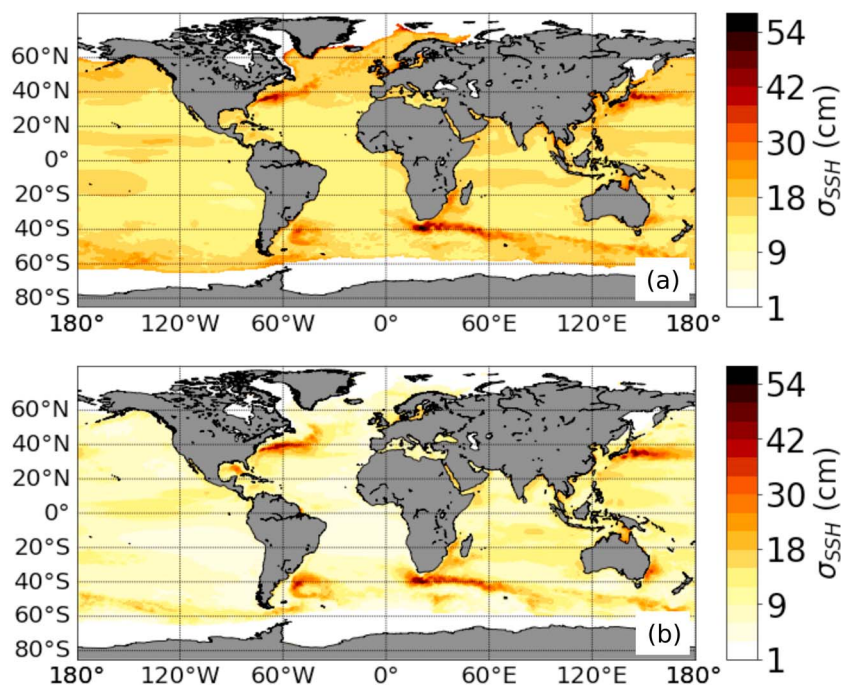


Figure 16. Sea surface height variability (cm) from (a) Energy Exascale Earth System Model version 1 high resolution (averaged over years 25 and 35 inclusive) and (b) AVISO.

et al., 2002). The mean and standard deviation for observational years 1979 to 2009 are shown and compared against the equivalent model years (280 to 310) for the fifth CORE cycle of model output for the EC60to30 resolution, and for years 1–37 of the RRS18to6 simulation. In the Northern Hemisphere there is generally good agreement between the model and observation, especially in winter, although E3SM overestimates sea ice extent in the Northern Hemisphere in summer. In the Southern Hemisphere, the model has too large a seasonal cycle compared to observations, although, again, agreement is generally good. Figure 13b compares total Northern Hemisphere sea ice volume between model output and the Pan-Arctic Ice Ocean Modeling and Assimilation System assimilated data product (Schweiger et al., 2011a). Interannual variance of ice volume is larger than ice area, but model and the Arctic Ice Ocean Modeling and Assimilation System product agree well, with the model capturing the seasonal cycle of sea ice volume. Due to a lack of reliable data product for the Southern Hemisphere, we only show model results for this region. Higher ice volume in the high-resolution simulation (Figure 13d) is expected due to the earlier CORE-II forcing years.

In Figures 14 and 15 we show spatial climatological maps of sea ice concentration for E3SM and for Special Sensor Microwave/Imager satellite observations, produced with the NASA Team algorithm (Cavalieri et al., 1996, updated yearly, 1996, updated yearly). Climatological maps are generated for the years 1979 to 2009 and for winter (January, February, and March in the Northern Hemisphere, and June, July, and August in the Southern Hemisphere) and summer (July, August, and September in the Northern Hemisphere, and December, January, and February in the southern hemisphere) seasons. In general, E3SM does a good job of reproducing the observational climatology of ice concentration and the ice pack edge. Good agreement is obtained in the Arctic during both seasons, especially during summer, with E3SM displaying too much ice in the Labrador and Greenland seas in winter. In the Southern Hemisphere, E3SM shows too much ice concentration in winter, whereas in summer the model displays too little ice in the Weddell Sea and virtually no sea ice along the East Antarctic coast ($60\text{--}160^{\circ}\text{E}$).

3.5. High-Resolution Diagnostics

The SSH variability averaged over 10 years of the E3SM run is shown in Figure 16 against the AVISO satellite product (Ablain et al., 2015). E3SM reproduces much of the observed SSH variability seen in observations. There are slight biases near the Agulhas, where eddy shedding is too regular, a common bias in eddy resolving ocean models (e.g., Maltrud & McClean, 2005). There is also too little variability in the Northwest Corner of the North Atlantic current. Finally, we note that the background SSH variability in E3SM is higher than

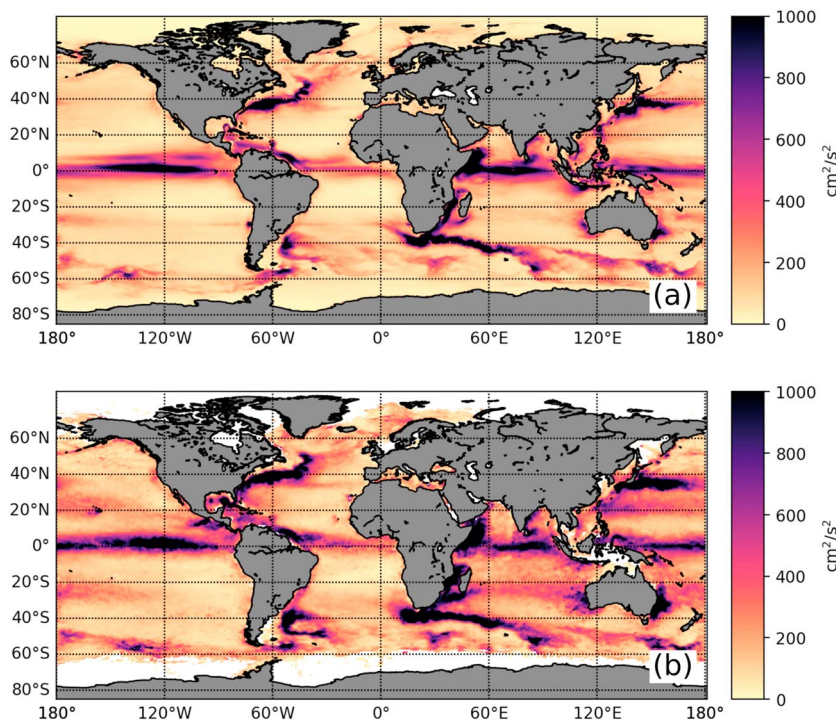


Figure 17. Eddy kinetic energy (cm^2/s^2) from (a) Energy Exascale Earth System Model version 1 high-resolution simulation (averaged over years 25–35). (b) Surface drifter climatology (Laurindo et al., 2017). SSH = sea surface height.

AVISO. This is most likely due to the split explicit time stepping in MPAS-Ocean, which does not filter gravity waves, whereas these waves are filtered by AVISO and implicit models of the barotropic component.

Figure 17 shows the eddy kinetic energy (EKE) averaged over years 25–35. E3SM EKE is higher than other eddy resolving ocean configurations. This is likely due to the improved, 80-layer, vertical grid used in E3SM, consistent with the results of Stewart et al. (2017). The distribution of EKE in the Northwest Corner of the high-resolution simulation compares well with observations.

4. Conclusions

This paper is one of many to present model configurations and simulation results for E3SM. Here we focus on coupled ocean and sea ice components, while others present results from stand-alone land ice (Hoffman et al., 2018), atmosphere (Tang et al., 2019), land surface (Ricciuto et al., 2018), and fully coupled simulations (Golaz et al., 2019). Model results demonstrate the ability of E3SM to produce realistic currents, MHT, sea ice coverage, and distributions of SST and salinity in this configuration where the atmosphere is CORE-II forcing. The high-resolution simulation shows the successful use of E3SM for strongly eddying flows, for example, for WBCs as well as the ACC. The solution fidelity for mesoscale dynamics in a multiresolution context will enable E3SM to resolve the mesoscale oceanic turbulence contributions to the global climate system in select regions of the global ocean instead of uniform high resolution.

Future applications employing enhanced regional refinement will provide novel directions of scientific inquiry. Many research topics will greatly benefit from the unique multiphysics and multiresolution capabilities of E3SM, including: coupled ocean-land-ice interactions; coastal studies of local sea level rise impacts; ocean-atmospheric feedbacks such as Eastern boundary current regions; and high-latitude dynamics, which are dependent upon a smaller Rossby radius of deformation. In the long term, variable-resolution meshes provide a lower computational cost, integrated approach to understanding localized climate impacts within the larger earth system. New algorithmic approaches will be needed to fully realize these efforts, particularly advanced time stepping approaches for variable-resolution meshes such that the model time step is not dictated by the smallest cell size, improved, scale-aware, sub-grid scale parameterizations, and performance optimization for unstructured meshes on new architectures. Current research by the authors and their col-

laborators is already making inroads in these areas, with the goal of near-term, measurable improvements in E3SM.

Most IPCC-class coupled climate models have had decades of development to reach their current level of fidelity and efficiency. As a brand new model, E3SM will have ample opportunity for improvement in the coming years but has already shown proficiency in computational performance and in reproducing twentieth-century climate. These initial simulations with standard configurations are just the first step. E3SM's multiresolution approach to global and regional climate modeling paves the way to a better understanding of the changing earth system at both the large and small scales.

Acknowledgments

This research was supported as part of the Energy Exascale Earth System Model (E3SM) project, funded by the U.S. Department of Energy, Office of Science, Office of Biological and Environmental Research. E3SM simulations are conducted at Argonne Leadership Computing Facility (contract DE-AC02-06CH11357); National Energy Research Scientific Computing Center (DE-AC02-05CH11231); Oak Ridge Leadership Computing Facility (DE-AC05-00OR22725); Argonne National Laboratory high-performance computing cluster, provided by BER Earth System Modeling; and Los Alamos National Laboratory Institutional Computing, U.S. DOE NNSA (DE-AC02-05CH11231). E3SM data are freely available through the Earth System Grid Federation (ESGF) distributed archives. See details at <https://e3sm.org/data> website.

References

- Abernathey, R., Cerovecki, I., Holland, P. R., Newsom, E., Mazloff, M., & Talley, L. D. (2016). Southern Ocean water mass transformation driven by sea ice. *Nature Geoscience*, 9, 596–601. <https://doi.org/10.1038/ngeo2749>
- Ablain, M., Cazenave, A., Larnicol, G., Balmaseda, M., Cipollini, P., Faugère, Y., et al. (2015). Improved sea level record over the satellite altimetry era (1993–2010) from the Climate Change Initiative project. *Ocean Science*, 11(1), 67–82. <https://doi.org/10.5194/os-11-67-2015>
- Adcroft, A., & Campin, J.-M. (2004). Rescaled height coordinates for accurate representation of free-surface flows in ocean circulation models. *Ocean Modelling*, 7, 269–284. <https://doi.org/10.1016/j.ocemod.2003.09.003>
- Amante, C., & Eakins, B. W. (2009). ETOPO1 1 arc-minute global relief model: Procedures, data sources and analysis (NOAA Technical Memorandum NESDIS NGDC-24). Boulder, CO: National Geophysical Data Center, NOAA. <https://doi.org/10.7289/V5C8276M>
- Arakawa, A., & Lamb, V. R. (1977). Computational design of the basic dynamical processes of the UCLA General Circulation Model. In J. Chang (Ed.), *Methods in computational physics: Advances in research and applications, General Circulation Models of the atmosphere* (Vol. 17, pp. 173–265). Amsterdam: Elsevier. <https://doi.org/10.1016/B978-0-12-460817-7.50009-4>
- Asay-Davis, X. S., Jourdain, N. C., & Nakayama, Y. (2017). Developments in simulating and parameterizing interactions between the Southern Ocean and the Antarctic Ice Sheet. *Current Climate Change Reports*, 3(4), 316–329. <https://doi.org/10.1007/s40641-017-0071-0>
- Bitz, C. M., & Lipscomb, W. H. (1999). An energy-conserving thermodynamic model of sea ice. *Journal of Geophysical Research*, 104(C7), 15,669–15,677. <https://doi.org/10.1029/1999JC900100>
- Briegleb, B. P., & Light, B. (2007). A Delta-Eddington multiple scattering parameterization for solar radiation in the sea ice component of the Community Climate System Model (Tech. Rep. NCAR/TN-472+STR). Boulder, CO: National Center for Atmospheric Research.
- Bryden, H. L., & Beal, L. M. (2001). Role of the Agulhas Current in Indian Ocean circulation and associated heat and freshwater fluxes. *Deep Sea Research Part I: Oceanographic Research Papers*, 48(8), 1821–1845. [https://doi.org/10.1016/S0967-0637\(00\)00111-4](https://doi.org/10.1016/S0967-0637(00)00111-4)
- Cavalieri, D. J., & Parkinson, C. L. (2012). Arctic sea ice variability and trends, 1979–2010. *The Cryosphere*, 6(4), 881–889. <https://doi.org/10.5194/tc-6-881-2012>
- Cavalieri, D. J., Parkinson, C. L., Gloersen, P., & Zwally, H. J. (1996, updated yearly). Sea ice concentrations from Nimbus-7 SMMR and DMSP SSM/I-SSMIS passive microwave data, version 1 (Tech. Rep.). Boulder, CO: NASA National Snow and Ice Data Center Distributed Active Archive Center. <https://doi.org/10.5067/8GQ8LZQVL0VL>
- Chen, Q., Ringler, T., & Gent, P. R. (2016). Extending a potential vorticity transport eddy closure to include a spatially-varying coefficient. *Computers & Mathematics with Applications*, 71(11), 2206–2217. <https://doi.org/10.1016/j.camwa.2015.12.041>, proceedings of the conference on Advances in Scientific Computing and Applied Mathematics A special issue in honor of Max Gunzburger's 70th birthday.
- Craig, A. P., Vertenstein, M., & Jacob, R. (2012). A new flexible coupler for earth system modeling developed for CCSM4 and CESM1. *The International Journal of High Performance Computing Applications*, 26(1), 31–42. <https://doi.org/10.1177/1094342011428141>
- Danabasoglu, G., Yeager, S. G., Bailey, D., Behrens, E., Bentsen, M., Bi, D., et al. (2014a). North Atlantic simulations in Coordinated Ocean-ice Reference Experiments phase II (CORE-II). Part I: Mean states. *Ocean Modelling*, 73, 76–107. <https://doi.org/10.1016/j.ocemod.2013.10.005>
- Danabasoglu, G., Yeager, S. G., Bailey, D., Behrens, E., Bentsen, M., Bi, D., et al. (2014b). North Atlantic simulations in Coordinated Ocean-ice Reference Experiments phase II (CORE-II). Part I: Mean states. *Ocean Modelling*, 73, 76–107. <https://doi.org/10.1016/j.ocemod.2013.10.005>
- Danabasoglu, G., Yeager, S. G., Kim, W. M., Behrens, E., Bentsen, M., Bi, D., et al. (2016). North Atlantic simulations in Coordinated Ocean-ice Reference Experiments phase II (CORE-II). Part II: Inter-annual to decadal variability. *Ocean Modelling*, 97, 65–90. <https://doi.org/10.1016/j.ocemod.2015.11.007>
- Dasgupta, G. (2003). Interpolants within Convex Polygons: Wachpress' Shape Functions. *Journal of Aerospace Engineering*, 16, 1–8. [https://doi.org/10.1061/\(ASCE\)0893-1321\(2003\)16:1\(1\)](https://doi.org/10.1061/(ASCE)0893-1321(2003)16:1(1))
- de Boyer Montégut, C., Madec, G., Fischer, A. S., Lazar, A., & Iudicone, D. (2004). Mixed layer depth over the global ocean: An examination of profile data and a profile-based climatology. *Journal of Geophysical Research*, 109, C12003. <https://doi.org/10.1029/2004JC002378>
- Donohue, K. A., Tracey, K. L., Watts, D. R., Chidichimo, M. P., & Chereskin, T. K. (2016). Mean Antarctic Circumpolar Current transport measured in Drake Passage. *Geophysical Research Letters*, 43, 11,760–11,767. <https://doi.org/10.1002/2016GL070319>
- Downes, S. M., Farneti, R., Uotila, P., Griffies, S. M., Marsland, S. J., Bailey, D., et al. (2015). An assessment of Southern Ocean water masses and sea ice during 1988–2007 in a suite of interannual CORE-II simulations. *Ocean Modelling*, 94, 67–94. <https://doi.org/10.1016/j.ocemod.2015.07.022>
- Dukowicz, J. K., & Baumgardner, J. R. (2000). Incremental Remapping as a Transport/Advection Algorithm. *Journal of Computational Physics*, 160(1), 318–335. <https://doi.org/10.1006/jcph.2000.6465>
- E3SM Project, DOE (2018). Energy Exascale Earth System Model. <https://doi.org/10.11578/E3SM/dc.20180418.36>
- Evans, K., Lauritzen, P., Mishra, S., Neale, R., Taylor, M., & Tribbia, J. (2013). AMIP simulation with the CAM4 spectral element dynamical core. *Journal of Climate*, 26(3), 689–709.
- Fretwell, P., Pritchard, H. D., Vaughan, D. G., Bamber, J. L., Barrand, N. E., Bell, R., et al. (2013). Bedmap2: Improved ice bed, surface and thickness datasets for Antarctica. *The Cryosphere*, 7(1), 375–393. <https://doi.org/10.5194/tc-7-375-2013>
- Ganachaud, A. (2003). Large-scale mass transports, water mass formation, and diffusivities estimated from World Ocean Circulation Experiment (WOCE) hydrographic data. *Journal of Geophysical Research*, 108(C7), 3213. <https://doi.org/10.1029/2002JC001565>

- Ganachaud, A., & Wunsch, C. (2000). Improved estimates of global ocean circulation, heat transport and mixing from hydrographic data. *Nature*, 408(6811), 453–457. <https://doi.org/10.1038/35044048>
- Gent, P. R., & Danabasoglu, G. (2011). Response to increasing Southern Hemisphere winds in CCSM4. *Journal of Climate*, 24(19), 4992–4998. <https://doi.org/10.1175/JCLI-D-10-05011.1>
- Gent, P. R., & McWilliams, J. C. (1990). Isopycnal mixing in ocean circulation models. *Journal of Physical Oceanography*, 20(1), 150–155. [https://doi.org/10.1175/1520-0485\(1990\)020<0150:IMIOC>2.0.CO;2](https://doi.org/10.1175/1520-0485(1990)020<0150:IMIOC>2.0.CO;2)
- Golaz, J.-C., Caldwell, P. M., Van Roekel, L. P., Petersen, M. R., Tang, Q., Wolfe, J. D., et al. (2019). The DOE E3SM coupled model version 1: Overview and evaluation at standard resolution. *Journal of Advances in Modeling Earth Systems*, 11. <https://doi.org/10.1029/2018MS001603>
- Griffies, S. M., Biastoch, A., Böning, C., Bryan, F., Danabasoglu, G., Chassignet, E. P., et al. (2009). Coordinated Ocean-ice Reference Experiments (COREs). *Ocean Modelling*, 26(1–2), 1–46. <https://doi.org/10.1016/j.ocemod.2008.08.007>
- Griffies, S. M., Danabasoglu, G., Durack, P. J., Adcroft, A. J., Balaji, V., Böning, C. W., et al. (2016). Omip contribution to CMIP6: Experimental and diagnostic protocol for the physical component of the Ocean Model Intercomparison Project. *Geoscientific Model Development*, 9(9), 3231–3296. <https://doi.org/10.5194/gmd-9-3231-2016>
- Griffies, S. M., Yin, J., Durack, P. J., Goddard, P., Bates, S. C., Behrens, E., et al. (2014). An assessment of global and regional sea level for years 1993–2007 in a suite of interannual CORE-II simulations. *Ocean Modelling*, 78, 35–89. <https://doi.org/10.1016/j.ocemod.2014.03.004>
- Hare, S. R., & Mantua, N. J. (2000). Empirical evidence for North Pacific regime shifts in 1977 and 1989. *Progress in Oceanography*, 47(2), 103–145. [https://doi.org/10.1016/S0079-6611\(00\)00033-1](https://doi.org/10.1016/S0079-6611(00)00033-1)
- Hoffman, M. J., Perego, M., Price, S. F., Lipscomb, W. H., Zhang, T., Jacobsen, D., et al. (2018). MPAS-Albany Land Ice (MALI): A variable-resolution ice sheet model for Earth system modeling using Voronoi grids. *Geoscientific Model Development*, 11(9), 3747–3780. <https://doi.org/10.5194/gmd-11-3747-2018>
- Holland, M. M., Bailey, D. A., Briegleb, B. P., Light, B., & Hunke, E. (2012). Improved sea ice shortwave radiation physics in CCSM4: The impact of melt ponds and aerosols on Arctic Sea Ice. *Journal of Climate*, 25(5), 1413–1430. <https://doi.org/10.1175/JCLI-D-11-00078.1>
- Holte, J., Talley, L. D., Gilson, J., & Roemmich, D. (2017). An Argo mixed layer climatology and database. *Geophysical Research Letters*, 44, 5618–5626. <https://doi.org/10.1002/2017GL073426>
- Hunke, E. C., & Dukowicz, J. K. (1997). An elastic-viscous-plastic model for sea ice dynamics. *Journal of Physical Oceanography*, 27(9), 1849–1867. [https://doi.org/10.1175/1520-0485\(1997\)027<1849:AEVPMF>2.0.CO;2](https://doi.org/10.1175/1520-0485(1997)027<1849:AEVPMF>2.0.CO;2)
- Hunke, E. C., & Dukowicz, J. K. (2002). The elastic-viscous-plastic sea ice dynamics model in general orthogonal curvilinear coordinates on a sphere—Incorporation of metric terms. *Monthly Weather Review*, 130(7), 1848–1865. [https://doi.org/10.1175/1520-0493\(2002\)130<1848:TEVPSI>2.0.CO;2](https://doi.org/10.1175/1520-0493(2002)130<1848:TEVPSI>2.0.CO;2)
- Hunke, E. C., Hebert, D. A., & Lecomte, O. (2013). Level-ice melt ponds in the Los Alamos sea ice model, CICE. *Ocean Modelling*, 71, 26–42. <https://doi.org/10.1016/j.ocemod.2012.11.008>
- Hunke, E. C., Lipscomb, W. H., Turner, A. K., Jeffery, N., & Elliott, S. (2015). CICE: The Los Alamos sea ice model documentation and software user's manual version 5.1 (Tech. Rep.). Los Alamos, NM: Los Alamos National Laboratory.
- Hurrell, J. W., Hack, J. J., Shea, D., Caron, J. M., & Rosinski, J. (2008). A new sea surface temperature and sea ice boundary dataset for the Community Atmosphere Model. *Journal of Climate*, 21(19), 5145–5153. <https://doi.org/10.1175/2008JCLI2292.1>
- Jacobsen, D. W., Gunzburger, M., Ringler, T., Burkhardt, J., & Peterson, J. (2013). Parallel algorithms for planar and spherical Delaunay construction with an application to centroidal Voronoi tessellations. *Geoscientific Model Development*, 6(4), 1353–1365. <https://doi.org/10.5194/gmd-6-1353-2013>
- Johns, W. E., Townsend, T. L., Fratantoni, D. M., & Wilson, W. D. (2002). On the Atlantic inflow to the Caribbean Sea. *Deep Sea Research Part I: Oceanographic Research Papers*, 49(2), 211–243. [https://doi.org/10.1016/S0967-0637\(01\)00041-3](https://doi.org/10.1016/S0967-0637(01)00041-3)
- Killworth, P. D. (1983). Deep convection in the World Ocean. *Reviews of Geophysics*, 21(1), 1–26. <https://doi.org/10.1029/RG021i001p00001>
- Kirtman, B. P., Bitz, C., Bryan, F., Collins, W., Dennis, J., Hearn, N., et al. (2012). Impact of ocean model resolution on CCSM climate simulations. *Climate Dynamics*, 39(6), 1303–1328.
- Large, W. G., McWilliams, J. C., & Doney, S. C. (1994). Oceanic vertical mixing—A review and a model with a nonlocal boundary-layer parameterization. *Reviews of Geophysics*, 32(4), 363–403.
- Large, W., & Yeager, S. (2009). The global climatology of an interannually varying airsea flux data set. *Climate Dynamics*, 33(2–3), 341–364. <https://doi.org/10.1007/s00382-008-0441-3>
- Laurindo, L. C., Mariano, A. J., & Lumpkin, R. (2017). An improved near-surface velocity climatology for the global ocean from drifter observations. *Deep Sea Research Part I: Oceanographic Research Papers*, 124, 73–92.
- Lipscomb, W. H. (2001). Remapping the thickness distribution in sea ice models. *Journal of Geophysical Research*, 106(C7), 13,989–14,000. <https://doi.org/10.1029/2000JC000518>
- Lipscomb, W. H., & Hunke, E. C. (2004). Modeling sea ice transport using incremental remapping. *Monthly Weather Review*, 132(6), 1341–1354. [https://doi.org/10.1175/1520-0493\(2004\)132<1341:MSITUI>2.0.CO;2](https://doi.org/10.1175/1520-0493(2004)132<1341:MSITUI>2.0.CO;2)
- Lipscomb, W. H., Hunke, E. C., Maslowski, W., & Jakacki, J. (2007). Ridging, strength, and stability in high-resolution sea ice models. *Journal of Geophysical Research*, 112, C03S91. <https://doi.org/10.1029/2005JC003355>
- Lipscomb, W. H., & Ringler, T. D. (2005). An incremental remapping transport scheme on a spherical geodesic grid. *Monthly Weather Review*, 133(8), 2335–2350. <https://doi.org/10.1175/MWR2983.1>
- Maltrud, M. E., & McClean, J. L. (2005). An eddy resolving global $1/10^\circ$ ocean simulation. *Ocean Modelling*, 8(1), 31–54. <https://doi.org/10.1016/j.ocemod.2003.12.001>
- Moore, J. K., Doney, S. C., & Lindsay, K. (2004). Upper ocean ecosystem dynamics and iron cycling in a global three-dimensional model. *Global Biogeochemical Cycles*, 18, GB4028. <https://doi.org/10.1029/2004GB002220>
- Moore, J. K., Lindsay, K., Doney, S. C., Long, M. C., & Misumi, K. (2013). Marine ecosystem dynamics and biogeochemical cycling in the Community Earth System Model [CESM1(BGC)]: Comparison of the 1990s with the 2090s under the RCP4.5 and RCP8.5 scenarios. *Journal of Climate*, 26(23), 9291–9312. <https://doi.org/10.1175/JCLI-D-12-00566.1>
- Nowlin, W. D., & Klinck, J. M. (1986). The physics of the Antarctic Circumpolar Current. *Reviews of Geophysics*, 24(3), 469–491. <https://doi.org/10.1029/RG024i003p00469>
- Parkinson, C. L., & Cavalieri, D. J. (2012). Antarctic sea ice variability and trends, 1979–2010. *The Cryosphere*, 6(4), 871–880. <https://doi.org/10.5194/tc-6-871-2012>
- Parkinson, C. L., Cavalieri, D. J., Gloersen, P., Zwally, H. J., & Comiso, J. C. (1999). Arctic sea ice extents, areas, and trends, 1978–1996. *Journal of Geophysical Research*, 104(C9), 20,837–20,856. <https://doi.org/10.1029/1999JC900082>

- Petersen, M. R., Jacobsen, D. W., Ringler, T. D., Hecht, M. W., & Maltrud, M. E. (2015). Evaluation of the arbitrary Lagrangian-Eulerian vertical coordinate method in the MPAS-Ocean model. *Ocean Modelling*, 86, 93–113. <https://doi.org/10.1016/j.ocemod.2014.12.004>
- Prinsenberg, S. J., & Hamilton, J. (2005). Monitoring the volume, freshwater and heat fluxes passing through Lancaster sound in the Canadian arctic archipelago. *Atmosphere-Ocean*, 43(1), 1–22. <https://doi.org/10.3137/ao.430101>
- Rauscher, S. A., Ringler, T. D., Skamarock, W. C., & Mirin, A. A. (2012). Exploring a global multiresolution modeling approach using Aquaplanet simulations. *Journal of Climate*, 26(8), 2432–2452. <https://doi.org/10.1175/JCLI-D-12-00154.1>
- Reckinger, S. M., Petersen, M. R., & Reckinger, S. J. (2015). A study of overflow simulations using MPAS-Ocean: Vertical grids, resolution, and viscosity. *Ocean Modelling*, 96, 291–313. <https://doi.org/10.1016/j.ocemod.2015.09.006>
- Ricciuto, D., Sargsyan, K., & Thornton, P. (2018). The impact of parametric uncertainties on biogeochemistry in the E3SM land model. *Journal of Advances in Modeling Earth Systems*, 10, 297–319. <https://doi.org/10.1002/2017MS000962>
- Redi, M. H. (1982). Oceanic isopycnal mixing by coordinate rotation. *Journal of Physical Oceanography*, 12(10), 1154–1158. [https://doi.org/10.1175/1520-0485\(1982\)012<1154:OIMBCR>2.0.CO;2](https://doi.org/10.1175/1520-0485(1982)012<1154:OIMBCR>2.0.CO;2)
- Ringler, T., & Gent, P. (2011). An eddy closure for potential vorticity. *Ocean Modelling*, 39(1), 125–34. <https://doi.org/10.1016/j.ocemod.2011.02.003>
- Ringler, T. D., Jacobsen, D., Gunzburger, M., Ju, L., Duda, M., & Skamarock, W. (2011). Exploring a multiresolution modeling approach within the shallow-water equations. *Monthly Weather Review*, 139(11), 3348–3368. <https://doi.org/10.1175/MWR-D-10-05049.1>
- Ringler, T., Petersen, M., Higdon, R. L., Jacobsen, D., Jones, P. W., & Maltrud, M. (2013). A multi-resolution approach to global ocean modeling. *Ocean Modelling*, 69, 211–232. <https://doi.org/10.1016/j.ocemod.2013.04.010>
- Ringler, T., Saenz, J. A., Wolfram, P. J., & Roekel, L. V. (2017). A thickness-weighted average perspective of force balance in an idealized circumpolar current. *Journal of Physical Oceanography*, 47(2), 285–302. <https://doi.org/10.1175/JPO-D-16-0096.1>
- Ringler, T. D., Thuburn, J., Klemp, J. B., & Skamarock, W. C. (2010). A unified approach to energy conservation and potential vorticity dynamics for arbitrarily-structured Cgrids. *Journal of Computational Physics*, 229(9), 3065–3090. <https://doi.org/10.1016/j.jcp.2009.12.007>
- Roach, A. T., Aagaard, K., Pease, C. H., Salo, S. A., Weingartner, T., Pavlov, V., & Kulakov, M. (1995). Direct measurements of transport and water properties through the Bering Strait. *Journal of Geophysical Research*, 100(C9), 18,443–18,457. <https://doi.org/10.1029/95JC01673>
- Roemmich, D. (1981). Circulation of the Caribbean Sea: A well-resolved inverse problem. *Journal of Geophysical Research*, 86(C9), 7993–8005. <https://doi.org/10.1029/JC086iC09p07993>
- Saenz, J. A., Chen, Q., & Ringler, T. (2015). Prognostic residual mean flow in an ocean general circulation model and its relation to prognostic Eulerian mean flow. *Journal of Physical Oceanography*, 45(9), 2247–2260. <https://doi.org/10.1175/JPO-D-15-0024.1>
- Schauer, U., Fahrbach, E., Osterhus, S., & Rohardt, G. (2004). Arctic warming through the Fram Strait: Oceanic heat transport from 3 years of measurements. *Journal of Geophysical Research*, 109, C06026. <https://doi.org/10.1029/2003JC001823>
- Schweiger, A., Lindsay, R., Zhang, J., Steele, M., Stern, H., & Kwok, R. (2011b). Uncertainty in modeled Arctic sea ice volume. *Journal of Geophysical Research*, 116, C00D06. <https://doi.org/10.1029/2011JC007084>
- Schweiger, A., Lindsay, R., Zhang, J., Steele, M., Stern, H., Kwok, R. (2011a). Uncertainty in modeled Arctic sea ice volume. *Journal of Geophysical Research*, 116, C00D06. <https://doi.org/10.1029/2011JC007084>
- Sein, D. V., Koldunov, N. V., Danilov, S., Wang, Q., Sidorenko, D., Fast, I., et al. (2017). Ocean modeling on a mesh with resolution following the local Rossby radius. *Journal of Advances in Modeling Earth Systems*, 9, 2601–2614. <https://doi.org/10.1002/2017MS001099>
- Skamarock, W. C., & Gassmann, A. (2011). Conservative transport schemes for spherical geodesic grids: High-order flux operators for ODE-based time integration. *Monthly Weather Review*, 139, 2962–2975. <https://doi.org/10.1175/MWR-D-10-05056.1>
- Skamarock, W. C., Klemp, J. B., Duda, M. G., Fowler, L. D., Park, S.-H., & Ringler, T. D. (2012). A multiscale nonhydrostatic atmospheric model using centroidal Voronoi Tesselations and C-grid staggering. *Monthly Weather Review*, 140(9), 3090–3105. <https://doi.org/10.1175/MWR-D-11-00215.1>
- Smith, R., Jones, P., Briegleb, B., Bryan, F., Danabasoglu, G., Dennis, J., et al. (2010). The Parallel Ocean Program (POP) reference manual: Ocean component of the Community Climate System Model (CCSM) (Tech. Rep.). Los Alamos, NM: Los Alamos National Laboratory.
- Sprintall, J., Wijffels, S. E., Molcard, R., & Jaya, I. (2009). Direct estimates of the Indonesian Throughflow entering the Indian Ocean: 2004–2006. *Journal of Geophysical Research*, 114, C07001. <https://doi.org/10.1029/2008JC005257>
- Steele, M., Morley, R., & Ermold, W. (2001). Phc: A global ocean hydrography with a high-quality Arctic Ocean. *Journal of Climate*, 14(9), 2079–2087. [https://doi.org/10.1175/1520-0442\(2001\)014<2079:PGOHW>2.0.CO;2](https://doi.org/10.1175/1520-0442(2001)014<2079:PGOHW>2.0.CO;2)
- Stewart, K. D., Haine, T. W. N., Hogg, A. M., & Roquet, F. (2017). On cabbeling and thermobaricity in the surface mixed layer. *Journal of Physical Oceanography*, 47(7), 1775–1787. <https://doi.org/10.1175/JPO-D-17-0025.1>
- Stocker, T. F., Qin, D., Plattner, G.-K., Tignor, M., Allen, S. K., Boschung, J., et al. (2013). Climate change 2013: The physical science basis (Tech. Rep.) (1535 pp.). One Liberty Plaza, New York: Cambridge University Press. <https://doi.org/10.1017/CBO9781107415324>
- Tang, Q., Klein, S. A., Xie, S., Lin, W., Golaz, J.-C., Roesler, E. L., et al. (2019). Regionally refined capability in E3SM Atmosphere Model Version 1 (EAMv1) and applications for highresolution modelling. *Geoscientific Model Development Discussions*, 2019, 1–36. <https://doi.org/10.5194/gmd-2019-11>
- Thuburn, J., Ringler, T. D., Skamarock, W. C., & Klemp, J. B. (2009). Numerical representation of geostrophic modes on arbitrarily structured C-grids. *Journal of Computational Physics*, 228(22), 8321–8335. <https://doi.org/10.1016/j.jcp.2009.08.006>
- Trenberth, K. E., & Caron, J. M. (2001). Estimates of meridional atmosphere and ocean heat transports. *Journal of Climate*, 14(16), 3433–3443. [https://doi.org/10.1175/1520-0442\(2001\)014<3433:EOMAAO>2.0.CO;2](https://doi.org/10.1175/1520-0442(2001)014<3433:EOMAAO>2.0.CO;2)
- Turner, A. K., & Hunke, E. C. (2015). Impacts of a mushy-layer thermodynamic approach in global sea-ice simulations using the CICE sea-ice model. *Journal of Geophysical Research: Oceans*, 120, 1253–1275. <https://doi.org/10.1002/2014JC010358>
- Turner, A. K., Hunke, E. C., & Bitz, C. M. (2013). Two modes of sea-ice gravity drainage: A parameterization for large-scale modeling. *Journal of Geophysical Research: Oceans*, 118, 2279–2294. <https://doi.org/10.1002/jgrc.20171>
- van der Werf, P. M., vanLeeuwen, P. J., Ridderinkhof, H., & de Ruijter, W. P. M. (2010). Comparison between observations and models of the Mozambique Channel transport: Seasonal cycle and eddy frequencies. *Journal of Geophysical Research*, 115, C02002. <https://doi.org/10.1029/2009JC005633>
- Van Roekel, L. P., Adcroft, A., Danabasoglu, G., Griffies, S. M., Kauffmann, B., Large, W. G., Levy, M., Reichl, B. G., Ringler, T., & Schmidt, M. (2018). The KPP boundary layer scheme for the ocean: Revisiting its formulation and benchmarking one-dimensional simulations relative to LES. *Journal of Advances in Modeling Earth Systems*, 10, 2647–2685. <https://doi.org/10.1029/2018MS001336>
- Whitworth, T., & Peterson, R. G. (1985). Volume transport of the Antarctic Circumpolar Current from bottom pressure measurements. *Journal of Physical Oceanography*, 15(6), 810–816. [https://doi.org/10.1175/1520-0485\(1985\)015<0810:VTOTAC>2.0.CO;2](https://doi.org/10.1175/1520-0485(1985)015<0810:VTOTAC>2.0.CO;2)
- Wolfram, P. J., & Ringler, T. D. (2017a). Quantifying residual, eddy, and mean flow effects on mixing in an idealized circumpolar current. *Journal of Physical Oceanography*, 47(8), 1897–1920. <https://doi.org/10.1175/JPO-D-16-0101.1>

- Wolfram, P. J., & Ringler, T. D. (2017b). Computing eddy-driven effective diffusivity using Lagrangian particles. *Ocean Modelling*, 118, 94–106. <https://doi.org/doi:10.1016/j.ocemod.2017.08.008>
- Wolfram, P. J., Ringler, T. D., Maltrud, M. E., Jacobsen, D. W., & Petersen, M. R. (2015). Diagnosing isopycnal diffusivity in an eddying, idealized midlatitude ocean basin via Lagrangian, In-situ, Global, High-Performance Particle Tracking (LIGHT). *Journal of Physical Oceanography*, 45(8), 2114–2133. <https://doi.org/10.1175/JPO-D-14-0260.1>
- Woodring, J., Petersen, M., Schmeißer, A., Patchett, J., Ahrens, J., & Hagen, H. (2016). In situ eddy analysis in a High-Resolution Ocean Climate Model. *IEEE Transactions on Visualization and Computer Graphics*, 22(1), 857–866. <https://doi.org/10.1109/TVCG.2015.2467411>
- Zwally, H. J., Comiso, J. C., Parkinson, C. L., Cavalieri, D. J., & Gloersen, P. (2002). Variability of Antarctic sea ice 1979–1998. *Journal of Geophysical Research*, 107(C5), 3041. <https://doi.org/10.1029/2000JC000733>